INVITED PAPER

Synchrophasor Sensor Networks for Grid Communication and Protection

This paper focuses on using synchrophasor data to improve the effectiveness of grid protection and reducing outages.

By Hamid Gharavi, *Fellow IEEE*, and Bin Hu, *Senior Member IEEE*

ABSTRACT | This paper focuses primarily on leveraging synchronized current/voltage amplitudes and phase angle measurements to foster new categories of applications, such as improving the effectiveness of grid protection and minimizing outage duration for distributed grid systems. The motivation for such an application arises from the fact that with the support of communication, synchronized measurements from multiple sites in a grid network can greatly enhance the accuracy and timeliness of identifying the source of instabilities. The paper first provides an overview of synchrophasor networks and then presents techniques for power quality assessment, including fault detection and protection. To achieve this we present a new synchrophasor data partitioning scheme that is based on the formation of a joint space and time observation vector. Since communication is an integral part of synchrophasor networks, the newly adopted wireless standard for machine-to-machine (M2M) communication, known as IEEE 802.11ah, has been investigated. The paper also presents a novel implementation of a hardware in the loop testbed for real-time performance evaluation. The purpose is to illustrate the use of both hardware and software tools to verify the performance of synchrophasor networks under more realistic environments. The testbed is a combination of grid network modeling, and an Emulab-based communication network. The combined grid and communication network is then used to assess power quality for fault detection and location using the IEEE 39-bus and 390-bus systems.

KEYWORDS | Emulab; fault detection and location; grid protection; IEEE 802.11ah; M2M; smart grid; synchrophasor networks; wireless networks; WLAN

Manuscript received September 14, 2016 ; revised December 13, 2016; accepted January 8, 2017. Date of publication May 19, 2017; date of current version June 16, 2017. *(Corresponding author: Bin Hu.)*

The authors are with the Advanced Network Technologies Division, National Institute of Standards and Technology, Gaithersburg, USA (e-mail: gharavi@nist.gov; bhu@nist.gov).

I. INTRODUCTION

A major challenge for future wide area measurement systems is how to respond securely and reliably to various disturbances in the next generation of power grid networks. An important aspect of grid protection is outage management that could prevent a cascading failure in the grid network. Synchronized phasor networks are currently used for wide area monitoring of transmission systems [1]–[5]. These networks consist of a number of phasor measurement units (PMUs), which are normally placed at sensitive locations throughout the transmission grid. Their optimal placement for transmission grid systems has received considerable attention by researchers in the past [6]–[10]. The main objective is to maximize the systems' observability with a minimal number of deployed PMUs. The number of PMUs in a large-scale deployment may also depend on the state estimation, which could require additional strategically placed PMUs to reduce vulnerability of the measurement system against noise [11]. By providing power flow analysis, state estimation can be used as a strong tool for monitoring the power system's prevailing conditions, as well as checking whether the estimated state variables are consistent with the measurements [12]–[15]. More importantly, timely estimation of the state variable at every point of the monitoring area is crucial for grid protection and control. Synchrophasor measurements can indeed provide real-time visibility to the dynamics of the power system that would complement traditional supervisory control and data acquisition (SCADA) measurements [16], [17]. Synchrophasor networks offer significant advantages by providing fast and precise measurement for voltage and current phasors throughout the grid system. This is mainly because for wide area monitoring systems

Digital Object Identifier: 10.1109/JPROC.2017.2696881

(WAMS), SCADA measurements are unable to provide a timely assessment of the system due to low sampling rates, as well as a lack of time synchronization [18].

While PMUs are mainly deployed for high-voltage power transmission, their feasibility for monitoring power quality and protection in a distribution system is gaining momentum [19]–[26]. Indeed, the need for rigorous power monitoring and protection is becoming more pertinent, particularly with the increasing amount of distributed energy resources (DERs) in customer premises [27]–[30]. These DERs, which include technologies such as photovoltaic (PV), wind generators, and storage, need operational management and control in the utility distribution system. Bear in mind that traditional distribution grids, which are based on passing power from bulk generators to consumers, face new challenges to manage and control the increasing penetration of DERs. As distribution moves quickly toward an active grid, ensuring balance and stability of grid monitoring in a timely manner requires extensive measurements through an experimental deployment of PMUs [31]. PMUs can be effectively used to estimate power quality by examining whether there is any stress that can impact grid stability. However, their deployment in a distribution system faces many obstacles, such as insufficient phasor measurement accuracies under noise and harmonics. In addition, the presence of volt-ampere-reactive (VAR) power can create serious instabilities due to the presence of nonlinear loads [32]–[36]. Because PMUs measure voltage and current phasors, they can directly compute real power and VAR flows at precise moments in time. More importantly, synchrophasor technology provides the status of a power system at a much faster rate than traditional power system state estimators or other similar measurement systems, such as SCADA [16], [17].

While synchronized phasor measurements may open the door to a new age of active distribution grids, the biggest obstacle is the lack of a communication network infrastructure, which is a key factor in supporting the grid protection system. Furthermore, to ensure balance and stability the communication infrastructure network should also support a vast number of sensors and actuators, which have different data traffic characteristics. Traditional distribution grid systems do not have the support of any communication infrastructure. Under these conditions, wireless networks are often viewed as the most cost-effective alternative to wireline communications. Recently, there has been a tremendous effort to promote the wireless-based Internet of Things (IoT), or simply M2M communications for wide ranging sensory devices [37]–[47]. For synchrophasor applications, however, the M2M-driven IoT will differ fundamentally from those considered for large-scale sensor networks. In particular, the realization of grid monitoring would require low delay and real-time communications. For instance, the bandwidth of a synchrophasor data, while depending on its reporting rate, may take up to several tens of kilobits per second (kb/s) per PMU node. Since there are always many other types of sensors and actuators that together can generate a large amount of data, a careful assessment of the overall bandwidth and delay requirements would be essential for future design and planning. Therefore, in this paper, we present a design framework for an end-to-end integrated grid/communication network for power quality assessment. Fig. 1 shows the overall structure of the grid and communication networks that will be the basis for our coverage. It consists of three distinct parts: grid networking that is based on synchrophasor technology for monitoring and protection, communication networking, and signal processing that is required for power quality monitoring and fault detection. For power quality classifications, we expand on the concept of the space–time partitioning introduced in our recent work [48]. The expansion is based on the formation of a joint space–time observation vector to perform a stable K-means clustering. In addition, for a collective assessment of these diverse entities, we also present a novel hardware in the loop testbed implementation for real-time monitoring. The testbed includes a grid network using commercial PMUs and a communication network based on an emulation platform. Furthermore, in order to evaluate a large network where deployment of commercial PMUs is not cost effective, we present a design of virtual PMUs (VPMUs) for real-time assessment of a grid monitoring system.

The paper is organized as follows. Section II describes the concept behind the synchrophasor network technology for grid monitoring and its potential applications for power quality assessment. We then present a communication networking strategy that is based on the emerging IEEE 802.11ah standard in Section III. Since this new standard was designed for wide ranging sensory applications, we particularly examine its suitability to meet the real-time requirements of synchrophasor networks, as well other sensory data for power quality monitoring and real-time fault detection. In Section IV, we present our proposed algorithms for power quality monitoring. Section V introduces our novel hardware in loop grid-communication testbed design that uses an emulation platform for communication networks and software-based synchrophasor grid networks for real-time evaluation of our proposed power quality monitoring scheme. Section V also presents an evaluation of the synchrophasor communication network and the results of our fault detection and location scheme.

II. ADVANCED GRID NETWORKS

Power system frequency is a good indicator of the systems' stability in alternating current (ac). Under ideal conditions the frequency should remain constant and close to the nominal frequency of 50 or 60 Hz. In reality, however, frequency of voltage and current signals tend to deviate from the nominal frequency due to a mismatch between generators and load. Under these conditions the calculation

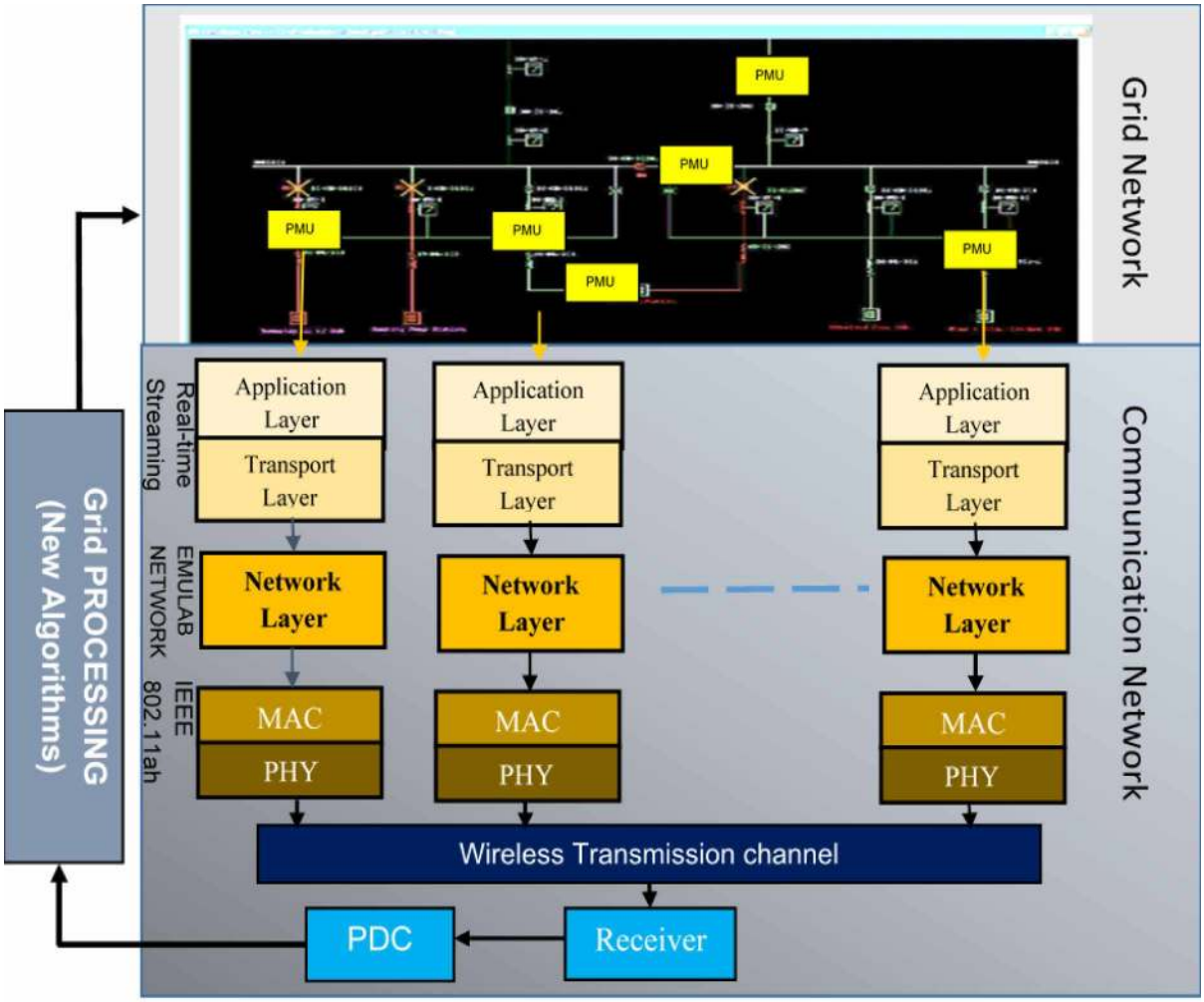

Fig. 1. ***Combined grid communication networks.***

of phase angle can be used to estimate the frequency of the system at the time of measurement. Thus, the basic concept behind the synchrophasor network is to place measuring devices at different locations on a grid in order to capture voltage and current waveforms using a standard time signal as the reference for measurement. This task can be accomplished by PMUs.

PMU measurements are obtained by first sampling the voltage and current waveforms using a global positioning system (GPS) and accurately time stamping each sample in order to provide a meaningful assessment of phase and amplitude variations across the grid. As shown in Fig. 2, the sampled data are then used to compute the corresponding 60- or 50-Hz phasor component as complex numbers representing the magnitude and phase angle of sinusoidal waveforms. As a result, synchrophasors measured across the power grid will have a common timing reference, hence can be used to assess power quality and, if necessary, provide an early warning of deteriorating system conditions.

A. Synchrophasor Grid Network

Synchrophasor measurements are envisioned to be a key enabler for real-time power grid situational awareness and control. PMU technology provides phasor information that captures a snapshot of the grid monitoring area in real time. These devices, which are dispersed throughout the grid system, measure the phase and voltage variation in buses to evaluate the degree of instability in the system. For example, as shown in Fig. 3, PMU devices can be installed within a bus/feeder where each PMU representing a communication node can send its measured data to the local phasor data collector (PDC).

Fig. 4 shows a general block diagram of a PMU using GPS signaling. Prior to analog-to-digital converter (ADC), electric waveforms are first passed through an anti-aliasing filter in order to restrict the bandwidth of input signals to satisfy the Nyquist–Shannon sampling theorem. Time tagging for synchronization is performed using the sampling

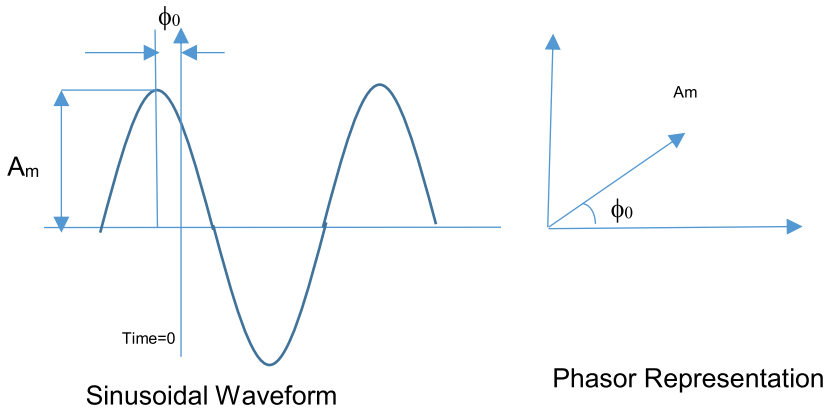

Fig. 2. ***Phasor representation of a sinusoidal waveform.***

clock provided by a GPS receiver. The basic idea of sampling electric waveforms using GPS is to examine phase and amplitude uncertainties, which affect the fundamental frequency that operates at a nominal rate of 60 or 50 Hz under normal conditions. GPS is mostly used to synchronize PMUs using a sampling clock, which is phase locked to one pulse per second (PPS). This can provide common and accurate timing referenced to coordinated universal time (UTC) [49], [50]. However, PMU may receive a synchronization signal from another source. For instance, an alternative synchronization solution is the IEEE 1588 synchronization module, which would provide timing accuracies better than 1 μs for devices connected via a network such as Ethernet. In particular, the IEC 61850-9-2 recommends Ethernet as a preferred communication, which supports the Precision Time Protocol (PTP) defined in the Standard IEEE 1588 [51], [52].

As shown in Fig. 4, the PMU functionally consists of two parts: measurement and data streaming for communications. Both have been defined separately by the IEEE C37.118-1 [49] and IEEE C37.118-2 [50] standards, respectively. Part-2 [50] of the standard deals with the communication aspects of the PMU by focusing on formats and data transfer between a PMU and a PDC as will be further discussed in Section III.

Part-1 [49] is mainly concerned with measurement of the synchrophasor parameters, PMU compliance, and testing conditions, particularly frequency and rate of change of frequency (ROCOF). While the standard does not recommend any specific algorithm for estimating these parameters, it defines total error vector (TVE) indices to evaluate frequency and ROCOF under particular conditions. It should be noted that the TVE represents the vector error

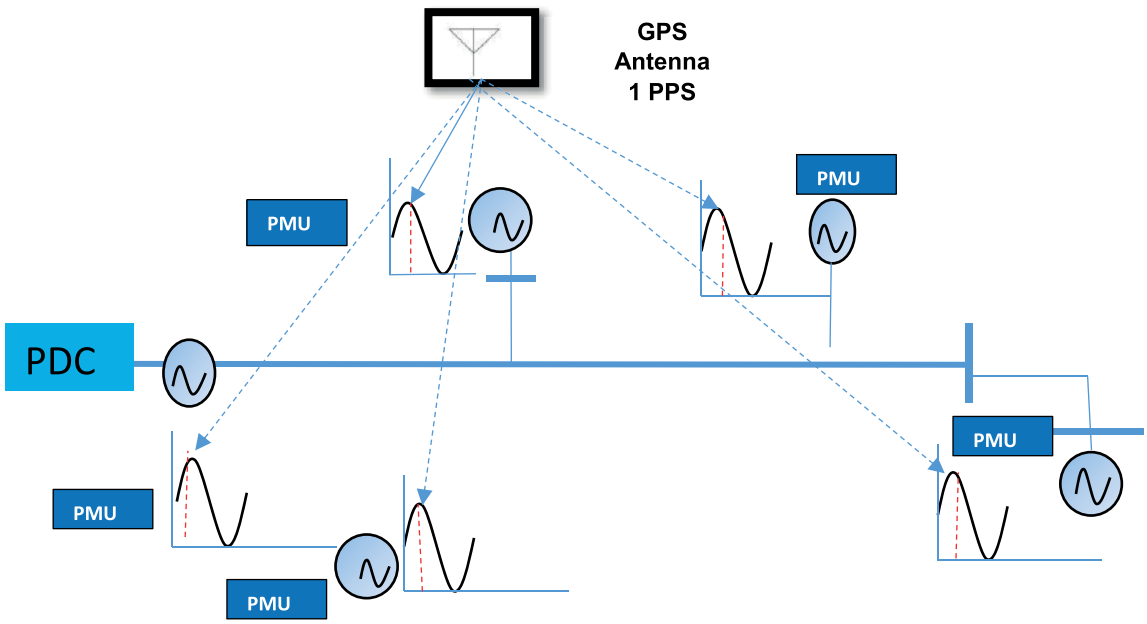

Fig. 3. ***Example of PMU deployment and communication within a small network.***

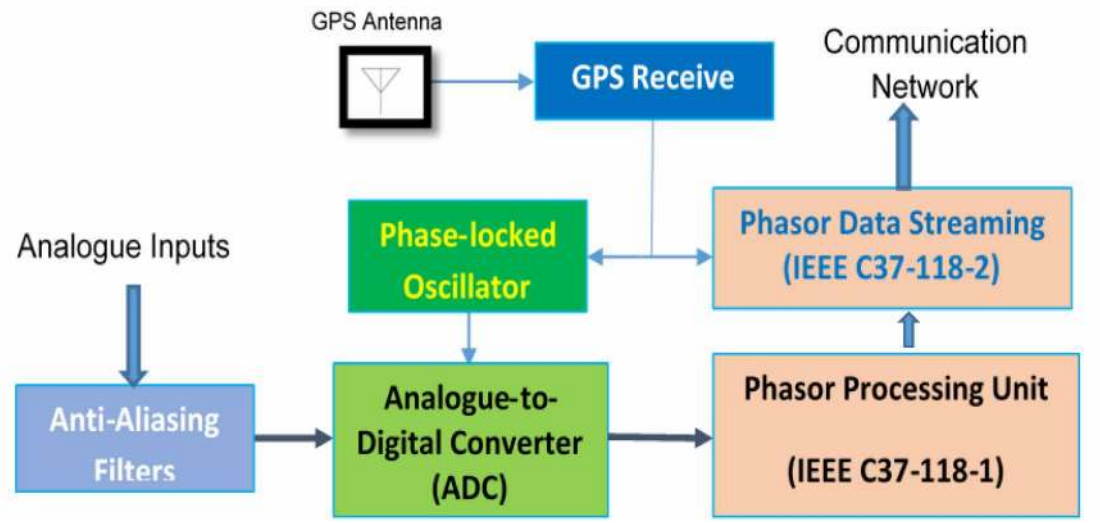

Fig. 4. ***Phasor measurement unit.***

between the theoretical and the estimated values. For example, a pure ac waveform can be represented as

$$x(t) = A_0 \cos(2\pi f_0 t + \phi_0) \tag{1}$$

where A_0, f_0, and ϕ_0 represent the magnitude of the sinusoidal waveform, instantaneous frequency, and phase angle relative to a cosine function at nominal system frequency synchronized to UTC, respectively. The corresponding phasor representation can be shown as [49]

$$X = \frac{A_0}{\sqrt{2}} e^{j\phi} = \frac{A_0}{\sqrt{2}} (\cos\phi + j \sin\phi) = X_r + jX_i \tag{2}$$

where X_r and X_i are real and imaginary components of the complex phasor representation. The TVE is defined as

$$\text{TVE} = \sqrt{\frac{(\overline{X}_r - X_r)^2 + (\overline{X}_i - X_i)^2}{X_r^2 + X_i^2}} \tag{3}$$

where $\overline{X}_r$ and $\overline{X}_i$ are real and imaginary components of the measured synchrophasor. For example, the Part-1 standard specifies that the TVE must be smaller than 1% for steady-state compliance and 3% for dynamic compliance under given testing conditions [49].

In addition, the standard defines two performance classes: P and M. The P-class is for protection application requiring a fast measurement response time and the M-Class is for high accuracy measurements with better filtering and a wider range of performance, without requiring the fastest reporting rate.

We should point out that a major factor that can affect the performance of the PMU is the presence of harmonics, which imposes many challenges in tracking the voltage and frequency variations. To incorporate harmonics, the nominal signal of voltage or current can be ideally represented by

$$x(t) = \sum_{i=0}^{H} A_i \cos(2\pi f_i t + \phi_i), \quad i = 0, 1, \ldots \tag{4}$$

where A_i, f_i, and ϕ_i correspond to the amplitude, frequency, and initial phase angle of the ith harmonics of the signal, respectively, and $i = 0$, f_0 represents the nominal frequency. Unfortunately, the signal in a real power system normally contains not only the harmonics, but also the decaying direct current (dc) offset generated by switches and faults in the power transmission lines, so the signal can be represented as

$$x(t) = \sum_{i=0}^{H} A_i \cos(2\pi f_i t + \phi_i) + I_{\text{dc}}{}^{-t/\tau} \tag{5}$$

where I_{dc} is the amplitude of decaying dc offset and τ is the time constant.

There are many schemes that have concentrated on estimating fundamental frequency f_0, as required by the IEEE C37.118 standard [49], [50]. A robust frequency estimation scheme should be capable of accurately tracing frequency variations, which is the key for reliable real-time monitoring, control, and protection. So far, many frequency estimation techniques, such as zero crossing [53], [54], a least squares error (LSE) technique [55], the Newton method [56], the Kalman filter [57]–[59], the Prony method [60], an artificial neural network [61], and a wavelet [62], [63], have been introduced. In addition, nonuniform sampling, such as log-time sampling [64], extended staggered undersampling [65], logarithmic sampling [66], and near-optimal sampling [67], have also been considered. One of the most widely used techniques to estimate phase and frequency is discrete Fourier transform (DFT) [53], [68]–[72]. The DFT-based frequency estimation technique is a commonly used algorithm because of its widespread signal processing applications and chip availability. For instance, to perform DFT, a rectangular window consisting of sample values for one cycle can be used to estimate the fundamental frequency. It is important to note that in electric power systems, frequency is constantly subjected to variations

of changes in supply and demand. This could consequently cause the fundamental frequency to deviate from its nominal 60 Hz by Δf (i.e., $f = f_0 + \Delta f$). Under these conditions, if the electric waveform is sampled at a fixed rate of an integer multiple of the nominal frequency (e.g., $f_s = 60 \times N$), the DFT would result in errors due to spectral leakage.

While there are specific requirements for the accuracy of frequency estimation by IEEE C37.118-1, a number of modifications were recently introduced in its 2014 amendment [73] for distributed systems. Nonetheless, it is unlikely that existing PMU products can provide accurate frequency estimation in the presence of noise and harmonics. In particular, the distribution system may also suffer from excessive reactive power. For these systems, the main challenge is how to regulate voltage and control the reactive power. With the help of a synchrophasor network this can be achieved in real time by measuring power factor (PF) in the vicinity of the installed distributed generation (DG) system with respect to the load impedance.

B. Power Factor (PF) Measurement via PMU

As shown in Fig. 5, the reactive power and the real power represent complex power where the imaginary axis and the real axis correspond to the reactive power and the real power of the vector diagram, respectively. The reactive power, which is measured in volt-amperes-reactive (VAR), causes the current to lag behind the voltage in phase. Voltage across a capacitor will oppose this change, causing the current to lead the voltage. When power systems have purely resistive loads, the power is called real power and is measured in watts. Apparent power is the magnitude of the complex power in kilovolt amperes (kVA). To ensure that the grid system will maintain voltage at the required level, the reactive power (either capacitive or inductive) needs to be measured and then adequately supplied by generators in the distribution system.

Let us assume that the voltage and current are purely sinusoidal, e.g.,

$$v(t) = V_0 \cos(2\pi f_0 t + \phi_0)$$
$$\text{and} \quad i(t) = I_0 \cos(2\pi f_0 t + (\phi_0 \pm \theta)). \tag{6}$$

As shown in Fig. 5, the complex power is the vector sum of active and reactive power where apparent power is the magnitude of the complex power, and the ratio between active power and apparent power is defined as PF

$$\text{PF} = \frac{P}{S} = \frac{1/T \int_0^T v(t)\, i(t)}{V_{RMS} * I_{RMS}} = \frac{V_{RMS} * I_{RMS}}{V_{RMS} * I_{RMS}} \cos(\theta). \tag{7}$$

Put simply, the PF is the cosine of the phase angle difference between voltage and current signals

$$\text{PF} = \cos(\theta). \tag{8}$$

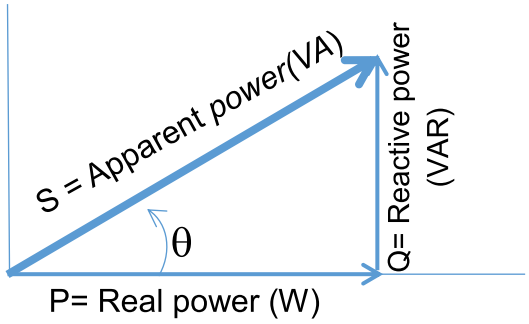

Fig. 5. ***Power triangle.***

In the presence of reactive power, the power factor drops below unity causing losses in the power system. Therefore, the PF is a good indicator of how effectively the current is being used in the supply system. Hence, in addition to phase, frequency, and ROCOF estimation, PF can be used to efficiently control the power system and ensure a balance between load and power generation. Since the PF also corresponds to the phase angle difference between voltage and current, its calculation relies heavily on the accuracy of the phase and frequency estimation and can be performed at regular intervals using PMUs. Currently, PMUs are being used for high voltage power transmission to measure voltage and current phase angles in synchronization with a GPS clock. However, using the synchrophasor data to calculate the PF may prove to be essential for distribution generation systems.

Unfortunately, in distribution systems, voltage and current may suffer from severe distortion and harmonics and measuring the phase difference between voltage and current waveforms will not be accurate enough. Instead, in the presence of harmonics, a true power factor (TPF) should be measured by taking into consideration the effect of harmonic distortion as defined below:

$$\text{TPF} = \text{DPF} * \text{DF(V)} * \text{DF(I)} \tag{9}$$

where DPF is the displacement power factor that corresponds to the cosine angle between the fundamental components of voltage and current. DF(V) and DF(I) are the distortion factors of voltage and current, respectively. For example, suppose the applied voltage is sinusoidal and the current contains harmonics

$$v(t) = V_0 \sqrt{2} \sin(\omega_0 t) \tag{10}$$

$$i(t) = I_1 \sqrt{2} \sin(\omega_0 t \pm \theta_1) + I_2 \sqrt{2} \sin(2\omega_0 t \pm \theta_2) \ldots . I_n \sqrt{2} \sin(n\omega_0 t \pm \theta_n). \tag{11}$$

Based on the above definitions, we can show

$$\text{DPF} = \cos\theta_1 \tag{12}$$

$$\text{DF(V)} = 1 \tag{13}$$

$$\mathrm{DF(I)} = \frac{I_1}{\sqrt{I_1^2 + I_2^2 + \cdots + I_n^2}}. \quad (14)$$

Total harmonic distortion (THD) is a common measurement of the level of harmonic distortion present in power systems and is defined as the ratio of total harmonics to the value of fundamental frequency

$$\mathrm{THD}_I = \frac{\sqrt{\sum_{j=2}^{n} I_j^2}}{I_1}. \quad (15)$$

We can show

$$\mathrm{DF(I)} = \frac{1}{\sqrt{1 + (\mathrm{THD}_I)^2}}. \quad (16)$$

Thus

$$\mathrm{TPF} = \frac{\cos(\theta_1)}{\sqrt{1 + (\mathrm{THD}_I)^2}}. \quad (17)$$

Note that PF and TPF calculation has been incorporated in our testbed design which uses VPMUs to assess the performance of large networks.

III. SYNCHROPHASOR COMMUNICATION NETWORKS

To establish an end-to-end communication link between PMU/PDC and PDC, the first step is to set up real-time message communications at the application layer based on the IEEE C37.118-2 standard. Fig. 6 shows commands and data exchange between a PMU and PDC for real-time communication [49], [74]. The command frame is used to turn the transmission on or off. There are three configuration frames (CFG) types, namely: CFG-1, CFG-2, and CFG-3. CFG-1 provides information about the full capabilities of a PMU (i.e., reporting rates, frequency range, noise suppression, etc.). CFG-2 denotes the currently reported measurements. CFG- 3 is optional and has a flexible frame format. The C37.118-2 has also specified a PDC-to-PDC communications protocol for a local PDC to send the aggregated data to the next level PDC (e.g., master PDC or utility PDC). Data frame formats for PMU-to-PDC and PDC-to-PDC are shown in Fig. 7(a) and (b), respectively. The PMU data frame includes current and voltage amplitudes, their synchronized phasor angles, frequency, as well as a ROCOF. Both PMU-to-PDC and PDC-to-PDC frames also include SYNC, frame size, identification code (i.e., ID code), a time stamp, which is specified as a SOC and fraction of second (FRACSEC) of the received data frame, bit-mapped flags (STAT), analog data (ANALOG), digital data (DIGITAL), and CTC check bits (CHK). A PDC, after it receives data from its associated PMUs within a predefined time period, will first align the frame according to the time stamps. In a two-level structure, each local PDC will then send the time aligned aggregated data to the master PDC (MPDC) at the utility control center. As can be easily deduced from Fig. 7(b), the PDC-to-PDC frame size will grow depending on the number of PMUs that report to each local PDC. A method that can reduce the PDC-to-PDC frame size has been investigated in [25].

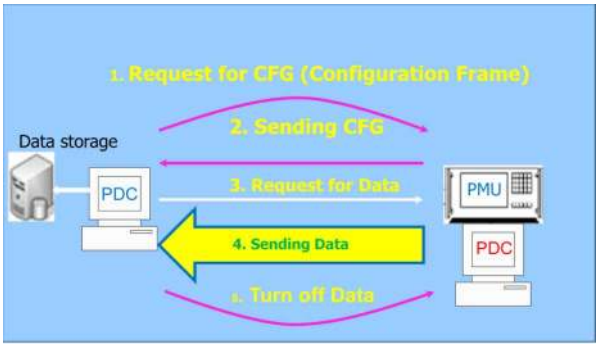

Fig. 6. *Commands and data exchange between PDC and PMU/PDC.*

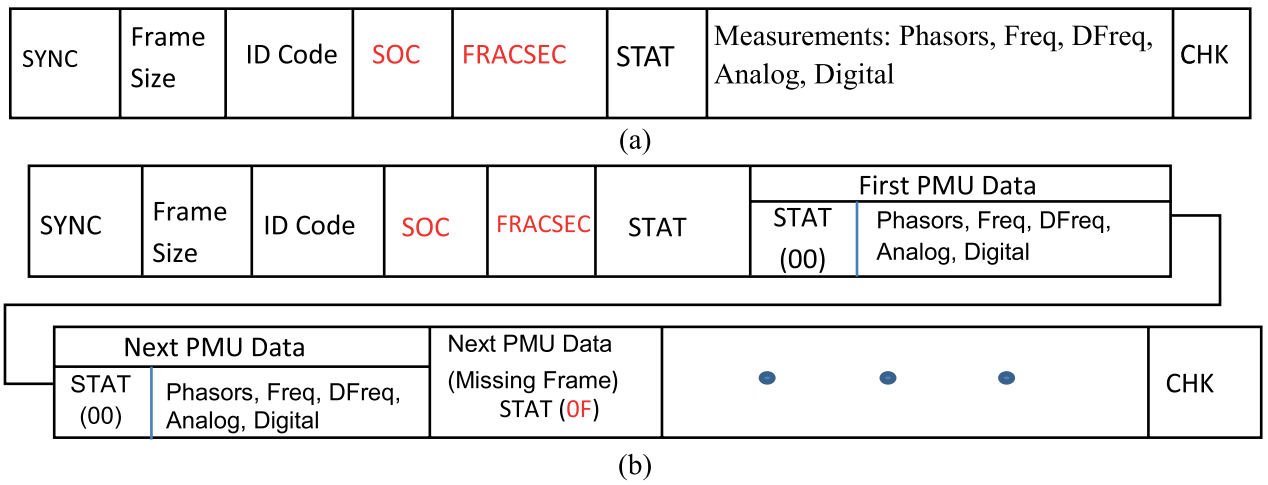

Fig. 7. *Data frame formats. (a) PMU-to-PDC. (b) PDC-to-PDC.*

A. M2M Wireless Network

PMU data streaming, which is built on top of the user datagram protocol over internet protocol (UDP/IP), needs to be transported to the PDC via a wireless network. The main challenge, however, is to find a suitable wireless access technology that can support not only the synchrophasor data in real time, but also other sensory data throughout the grid system. Generally, the development of new wireless communication networks for smart grid is dependent on the emergence of new standards. Recently, there has been a tremendous effort in promoting the wireless-based IoT, or simply M2M communication for wide ranging sensory devices. While the emerging fifth generation (5G) has envisioned a cellular-based network for IoT applications, a new wireless local area network (WLAN) standard, referred to as IEEE 802.11ah, is being introduced [75]–[80]. This aims to extend Wi-Fi applications in a sub-1-GHz spectrum.

Unlike other members of the IEEE 802.11 family of standards [81], [82] that operate in the unlicensed frequency bands of 2.4 and 5 GHz, the new IoT-centric 802.11ah extends Wi-Fi applications in a sub-1-GHz spectrum with carrier frequencies around 900 MHz and with coverage of up to 1 km outdoors [75]. The IEEE 802.11ah physical (PHY) layer is designed to increase spectral efficiency and system throughput, which is inherited from IEEE 802.11ac PHY [81]. It should be noted that in IEEE 802.11ah, 1- and 2-MHz channels are mandatory for all stations (STAs), while 4-, 8-, and 16-MHz channels are optional choices. For channels equal to or greater than 2 MHz, the PHY layer is exactly a ten-times downclocking version of 802.11ac's PHY layer. Similarly, orthogonal frequency-division multiplexing (OFDM), multiple-input–multiple-output (MIMO), and downlink multiuser MIMO (DL MU-MIMO) techniques are adopted by 802.11ah PHY. The duration of OFDM symbols is exactly ten times that in 802.11ac. The 802.11ah also supports the same set of modulation and coding schemes (MCSs), where binary shift keying (BPSK), quadrature shift keying (QPSK), and 16 to 256 quadrature amplitude modulation (QAM) modulations are employed.

The most important feature of IEEE 802.11ah is its ability to function in an efficient power saving mode. This makes it very attractive for low-data-rate, battery-powered wireless sensors. By adopting a 13-b hierarchical association identifier (AID) structure, the new standard can support up to 8191 ($2^{13} - 1$) devices on a single access point (AP), which would overcome one of the major challenges of the IoT to provide connectivity to a large number of battery-powered devices. More importantly, the AID hierarchical structure allows classification of each station (STA) according to the type of application, e.g., traffic pattern. Four hierarchical levels (page, block, sub-block, and station's index in sub-block) are used to compose the 13-b hierarchical AID, which is enclosed in the signaling beacons and is periodically broadcast by AP. The hierarchical structure

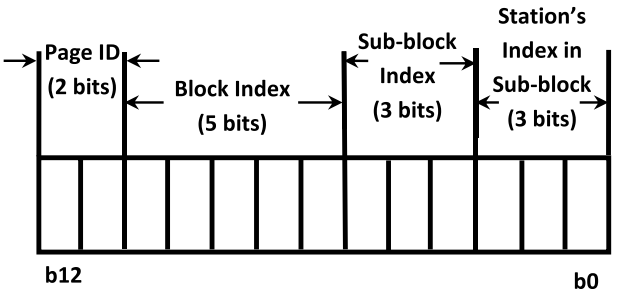

Fig. 8. *AID format for hierarchical addressing.*

can make it possible to group multiple STAs in a block or sub-block that can be identified simply by their block ID or sub-block ID (instead of all their AIDs). Grouping STAs can also be arranged in accordance with specific characteristics of the data (e.g., real time, non real time, delay sensitive, etc.), hence enabling more efficient utilization of wireless resources. Fig. 8 shows the AID format for hierarchical addressing.

Compared with other advanced low-power wireless network technologies, such as NB-IoT [82] that are primarily designed for low-date-rate applications, IEEE 802.11ah can support higher bandwidths and is therefore capable of handling synchrophasor communication. In addition, IEEE 802.11ah offers many other attractive features that are particularly suitable for grid monitoring and protection [83]. In this paper, we further expand the network for a grid system consisting of a large number of PMUs. For instance, the low delay requirement together with the nature of real time, as well as relatively high data rates of synchrophasor data, can put a tremendous constraint on the network. Addressing these constraints would require careful exploitation of the IEEE 802.11ah features, such as access grouping to handle not only the synchrophasor data, but also diverse categories of sensory information. Together with the hierarchical AID structure, our goal is to provide a low-delay, real-time communication between a PMU station and a PDC.

In this paper, a cellular topology is used for the wireless M2M sensor network, where a PDC represents an AP, while PMUs represent STAs. It is important to note that synchrophasor communication is mainly dominated by uplink data (i.e., PMU-to-PDC). Since PMU measurements are GPS synchronized at 1 PPS, they tend to transmit their data frames as soon as their measurements are complete. This could result in transmitting PMU data packets about the same time and cause severe contention. Furthermore, the low delay requirement together with real-time nature, and relatively high data rates of synchrophasor data, can put a tremendous strain on the network. Overcoming these constraints would require a careful exploitation of the IEEE 802.11ah capabilities. It should be noted that despite real-time operational requirements and its relatively upstream

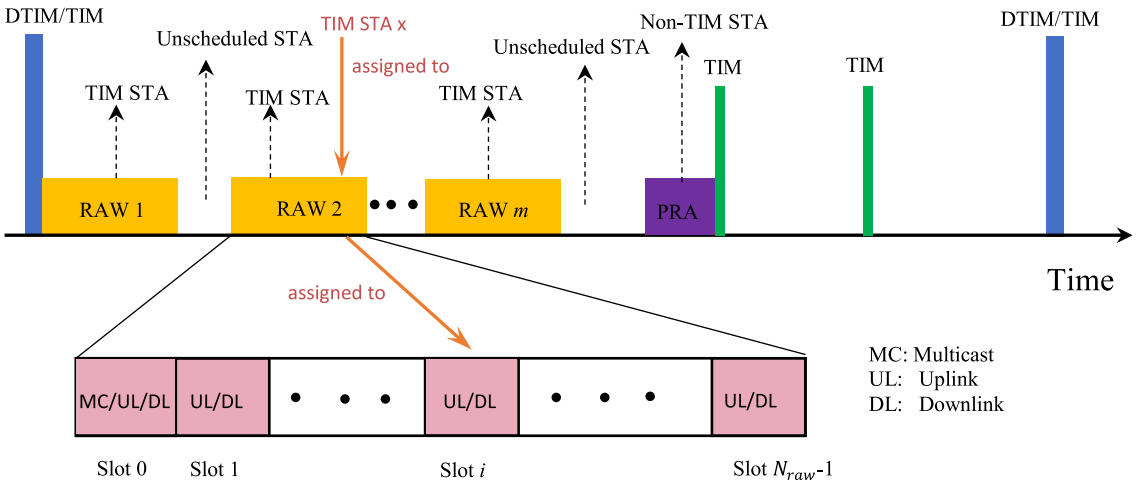

Fig. 9. ***IEEE 802.11ah channel access for TIM STA, non-time STA, and unscheduled STA.***

high data rates there exist many other low traffic sensory devises within power grid systems (especially distribution).

Indeed, IEEE 802.11ah has the ability to handle diverse categories of operational and nonoperational sensor data for power grid monitoring [83]. In particular, it offers an efficient power saving mechanism, which is based on a new traffic indication map (TIM) classification. For instance, the standard defines three types of stations: TIM station, non-TIM station, and unscheduled station. TIM stations have to listen to AP beacons to send or receive data within the new channel access method called restricted access window (RAW), whereas non-TIM stations can get permission from the AP for transmission through a periodic restricted access window (PRAW).The unscheduled stations can request sending data outside RAW by sending a poll frame to the AP at any time, hence they do not require to listen to any beacons to transmit data. As shown in Fig. 9, TIM STAs have to send and receive data within the assigned time slot of RAWs. This assignment is carried out by AP and transmitted to TIM STAs through periodic signaling beacons. For non-TIM STAs, periodic restricted access window (PRAW) is used to indicate periodically scheduled RAWs during which non-TIM STAs are permitted to transmit data. Unscheduled STAs do not listen to any beacon, instead they send request poll to their AP to gain channel access outside RAW. In 802.11ah, TIM signaling beacons are periodically transmitted by AP to inform STAs about the presence of buffered packets destined to each STA (see Fig. 10). As a special case of TIM, delivery TIM (DTIM) signaling beacons are used to indicate the existence of group addressed packets (i.e., multicast and broadcast packets) [84].

For synchrophasor applications, we consider PMUs as TIM stations using a TIM grouping structure. In each RAW duration only one group of PMU stations would be able to access the channel. Bear in mind that TIM stations access the channel using an enhanced distributed channel access (EDCA) operation which is based on transmission opportunity (TXOP). A TXOP is a bounded time interval where a PMU station can send a frame in real time as long as the period of the transmission is less than the specified duration. PMU stations receive the duration and start time of their RAW contention period via a beacon transmitted by the PDC (e.g., AP). These stations can then access the channel within each RAW period.

In TIM grouping a RAW can be assigned to one or more PMU stations. Since RAW can also be divided into a number of time slots, we consider three approaches for synchrophasor applications. In the first approach (configuration A) there is a single RAW within a TIM interval and all the PMUs are allocated to this single RAW, but each is assigned to a different slot (see Fig. 10). In the second approach (configuration B), a TIM interval consists of multiple RAWs, but each has a single time slot. In this configuration each slot is assigned to one PMU station. In the third approach (configuration C), a RAW with a single time slot is considered (see Fig. 10). Here all PMUs will compete to access the same slot.

Thanks to the flexibility of the new standard, the GPS synchronized data that are normally generated around the same time can be taken care of by the new RAW assignment—as long as they do not exceed the maximum selected IEEE 802.11ah capacity. For the sake of comparison, the total RAW duration in a DTIM interval for all three configurations is the same. The comparative results for all three configurations will be presented in Section V. In these scenarios, multiple PMUs periodically send synchrophasor measurements to a PDC (acting as AP) at specific frame rates, hence dominating uplink traffic (i.e., PMUs-to-PDC). Finally, we should point out that, apart from PMUs, the network should be able to handle other low-traffic volume

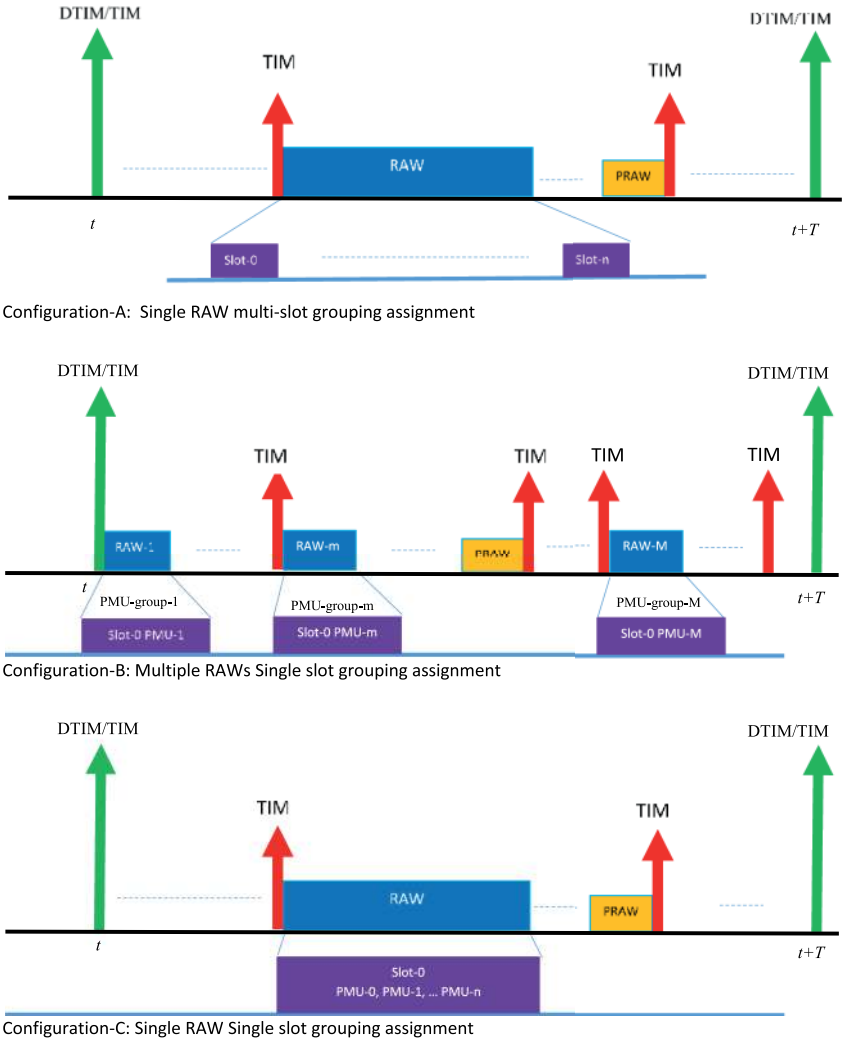

Fig. 10. ***Three approaches for real-time synchrophasor applications.***

sensory data. Such devices data can be considered as either non-TIM stations (using PRAW) or as unscheduled stations.

IV. POWER QUALITY ASSESSMENT AND FAULT DETECTION

The main objective of monitoring power quality in a distribution or transmission system is to allow grid operators to observe and detect disturbances almost as quickly as they occur. While power quality has many definitions, the main challenge is to develop methods that can effectively monitor voltage instability in order to provide timely protection against grid disturbances. Voltage instability may also be caused by faults, such as line tripping, short circuits, etc. In other words, voltage instability is a local phenomenon and any remedial action would require the support of a communication network with an integrated control strategy. Such a network should be able to provide access to a PMU wherever it is located. As described in the previous section, the M2M wireless network infrastructure is indeed capable of supporting communications between a PDC and its associated PMU. While IEEE 802.11ah can provide wireless access at the local level, the challenge is detecting and identifying the source of voltage instabilities at the local PDC level.

Therefore, our main aim is to develop a method to evaluate the link quality at the PDC level, where any protective control action can take place locally, rather than at the control center. As voltage fluctuations can also affect the power profile of neighboring regions, the objective is to identify a region between a pair of neighboring PMU nodes that suffers from a voltage fluctuation. For instance, a disturbance leading to a voltage collapse may be initiated by a variety of causes, such as a severe change of system conditions, or when the reactive power demand exceeds the sustainable capacity of the available reactive power resource. The presence of renewables can also contribute to voltage instability.

Indeed, there can be multiple sources of such instabilities caused by changing load demands, excessive reactive power, or faults.

In order to detect regions that have been impacted by voltage instability caused by faults or sudden overloads, we have considered *K*-means optimization [48]. It was shown that by selecting suitable observation vectors, the *K*-means approach would be able to classify the power quality into different clusters according to the degree of voltage instability. Two types of observation vectors (time and space) were proposed as the input. The time-based observation vector considers the consecutive time sample of each synchrophasor data (e.g., voltage) of PMU stations

$$V_i = [V_{t-n+1,i}, V_{t-n+2,i}, \ldots\ldots, V_{t,i}] \tag{18}$$

which has a dimension of n, where $t-n+1, t-n+2, \ldots, t$ corresponding to the n consecutive time stamps in which the synchrophasor data was measured. The space-based observation vector takes into consideration the position of PMU stations in order to detect multiple disturbances that may occur in different regions throughout the grid. The space-based observation vector for the ith node is a 2-D vector and can be expressed as

$$D_i = [D_{x,i}, D_{y,i}]. \tag{19}$$

To carry out both space and time optimization, a *K*-means clustering can be carried out in space and time via two consecutive stages where each stage uses its respective observation vector.

For instance, for a given m-dimensional observation vector $P_i = [V_1, V_2, \ldots\ldots, V_m]$ with K number of clusters $C = \{C_1, C_2, \ldots, C_K\}$, the *K*-means algorithm is run iteratively to minimize the error function defined as

$$E(V) = \sum_{i=1}^{K} \sum_{V \in C_i} \|\mu_i - V\|^2 \tag{20}$$

where C_i is the cluster with the centroid being μ_i.

The iteration process is done according to the following steps.

1) Select a set of K arbitrary n-dimensional center vectors within the observation vector domain.
2) Obtain the Euclidean distance between observation vectors and each cluster center.
3) Form a set of K clusters C_i $(i = 1, 2, \ldots, K)$ with the centroid being μ_i and map each observation vector to the nearest cluster center, where

$$C_i = \{V_k : \|\mu_i - V_k\|^2 \le \|\mu_j - V_k\|^2, 1 \le j \le K, j \ne i, \quad 1 \le k \le N\}. \tag{21}$$

4) Update the centroid of each cluster to represent a new set of cluster centers

$$\mu_i = 1/m_i \sum_{V_k \in C_i} V_k \tag{22}$$

where m_i is the number of observation vectors assigned to the cluster C_i.

5) Repeat steps 2)–4) until the assignments in each cluster remain unchanged.
6) Select the cluster with the longest distance to the positive sequence vector of the nonfaulted balanced system (i.e., $V_{\text{balance}} = [V_{t-n+1,i} = 1, V_{t-n+2,i} = 1, \ldots\ldots, V_{t,i} = 1]$) as the relatively most unstable cluster (MUC).

By replacing $P_i = [V_1, V_2, \ldots\ldots, V_m]$ with (18) for time and (19) for space, we can then form the inputs to the *K*-means clustering process, which are carried out separately based on each observation vector and in consecutive stages of merging and splitting clusters [48].

A. Proposed Space–Time Joint Observation Vector

The main deficiency of *K*-means clustering is that there is no guarantee to reach a global optimum solution. Therefore, to avoid the possibility of trapping into a local minima, in this paper, we expand the space–time optimization approach. The new approach is based on combining the space and time components into a single observation vector. The main challenge, however, is that the time-based synchrophasor components (i.e., $V_{t-n+1,i}, V_{t-n+2,} i, \ldots\ldots, V_{t,i}$) and the position-based components (i.e., $D_{x,i}, D_{y,i}$) have different characteristics and their integration into a single observation vector requires a rescaling of their components. To achieve this, we use the local-optima-free algorithm proposed in [85].

This Newton–Raphson-based algorithm, which will be referred to as global distance metric learning (GDML), uses a distance metric that exploits similarity and dissimilarity information from pairwise constraints. By processing metric learning as a convex optimization problem, the GDML algorithm can result in a highly stable clustering without merging to a local minimum.

Given a pair of points known to be similar $S{:}(x_i, x_j) \in S$ if x_i and x_j, the distance metric between the similar pair points x_i and x_j can be expressed as

$$\begin{aligned} d(x_i, x_j) = d_A(x_i, x_j) &= \|x_i - x_j\|_A \\ &= \sqrt{(x_i - x_j)^T A (x_i - x_j)} \end{aligned} \tag{23}$$

where A is a positive–semidefinite matrix. Metric learning is designed to minimize the squared distance between the similar pair points $(x_i, x_j) \in S$, to reflect their similarity. It can be expressed as the following optimization problem [85]:

$$\min_A \sum_{(x_i, x_j) \in S} \|x_i - x_j\|_A^2 \tag{24}$$

$$\text{s.t.} \sum_{(x_i, x_j) \in D} \|x_i - x_j\|_A \ge 1 \tag{25}$$

$$A \succcurlyeq 0 \tag{26}$$

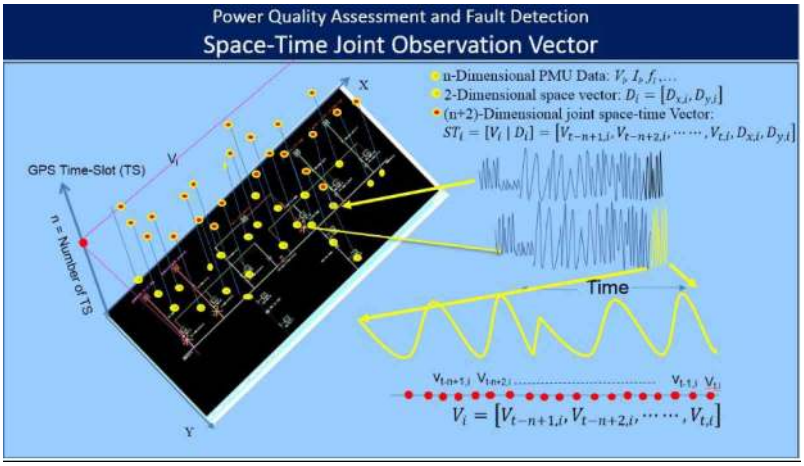

Fig. 11. ***Proposed space–time joint observation vector.***

where $S{:}(x_i, x_j) \in S$ if x_i and x_j are similar and $\mathcal{D}$ is a set of pairs of points known to be dissimilar. In the case of diagonal A, the Newton–Raphson method is then used to iteratively derive the matrix A [85], to solve the optimization problem in (24)–(26). It is important to note that GDML aims to find the weighting coefficients for rescaling the data $x \rightarrow A^{(1/2)}x$. The main objective is to move similar pairs closer to each other and dissimilar pairs as far away as possible. The rescaled data $A^{(1/2)}x$ is then processed by using K-means clustering. Because of this capability, we consider the GDML algorithm to rescale the space–time observation vector. As a result, the properly rescaled components can be used as a joint observation input to perform the above K-means for clustering.

For example, considering the n-dimensional time-based observation vector in (18) and a 2-D space-based observation vector in (19), the resulting $(n+2)$-dimensional joint space–time observation vector (see Fig. 11) can then be generated as

$$ST_i = [V_i \mid D_i] = [V_{t-n+1,i}, V_{t-n+2,i}, \ldots\ldots, V_{t,i}, D_{x,i}, D_{y,i}]. \quad (27)$$

For a grid system with an N number of PMUs, an observation matrix can be shown as

$$ST = \begin{bmatrix} ST_1 \\ ST_2 \\ \vdots \\ ST_N \end{bmatrix} = \begin{bmatrix} V_{t-n+1,1} & V_{t-n+2,1} & \cdots & V_{t,1} & D_{x,1} & D_{y,1} \\ V_{t-n+1,2} & V_{t-n+2,2} & \cdots & V_{t,2} & D_{x,2} & D_{y,2} \\ \vdots & \vdots & \ddots & \vdots & \vdots & \vdots \\ V_{t-n+1,N} & V_{t-n+2,N} & \cdots & V_{t,N} & D_{x,N} & D_{y,N} \end{bmatrix}. \quad (28)$$

Forming similarity pairs such as ST_i is similar to ST_j if $\|V_i - V_j\| < V_{\text{threshold}}$ and $\|D_i - D_j\| < D_{\text{threshold}}$. Otherwise, ST_i is dissimilar to ST_j. Based on the similarity and dissimilarity information, a similarity matrix $\mathbb{S}$ and a dissimilarity matrix $\mathbb{D}$ can be formed, where $\mathbb{S}_{ij} = 1$ if ST_i is similar to ST_j while $\mathbb{D}_{ij} = 1$ if ST_i is dissimilar to ST_j. Note that not all similarity and dissimilarity information would be needed to derive the rescaled matrix A [85].

The observation matrix ST, together with similarity matrix $\mathbb{S}$ and dissimilarity matrix $\mathbb{D}$, is used to derive the rescale matrix A by employing the Newton–Raphson method to solve the optimization problem in (24)–(26), where [85]

$$g(A) = g(A_{11}, \ldots, A_{(n+2)(n+2)}) = \sum_{(ST_i, ST_j) \in \mathbb{S}} \|ST_i - ST_j\|_A^2 - \log\left(\sum_{(ST_i, ST_j) \in \mathcal{D}} \|ST_i - ST_j\|_A\right). \quad (29)$$

A K-means algorithm is then used to cluster the rescaled observation matrix $Y = ST * A(1/2)$.

After K-means clustering, the standard deviation of each cluster is calculated to ensure that it does not contain any unstable vectors. For cluster $C_k (k = 1, 2, \ldots, K)$ with centroid μ_k, the standard deviation can be expressed as

$$SD_k = \sqrt{\frac{1}{m_k(n+2)} \sum_{Y_i \in C_k} \|Y_i - \mu_k\|^2} \quad (30)$$

where m_k is the number of rescaled observation vectors assigned to the cluster C_k. If $SD_k \geq SD_{\text{threshold}}$, K-means clustering will be repeated on cluster C_k to locate the unstable (e.g., faulty) links. Otherwise, C_k will be labeled as stable if it contains enough rescaled observation vectors (i.e., $m_k > m_{\text{threshold}}$). Bear in mind that for a small cluster the value of SD_k may fall below the $SD_{\text{threshold}}$ despite having an unstable link(s). Therefore, for any such cluster, further K-means partitioning will be carried out by generating new clusters $\overline{C}_k$ using only a set of time-based observation vectors: V_i $(I = 1, 2, \ldots, m_k)$ that correspond to $Y_i \in C_k$ (see Fig. 12). More precisely, a cluster with the longest distance to the V_{balance} vector (i.e., $V_{\text{balance}} = [V_{t-n+1,} =_{1,i} V_{t-n+2,i} = 1, \ldots\ldots, V_{t,i} = 1]$) is considered as the MUC, otherwise it will be marked as stable. If the MUC contains more than two voltage-based observation vectors,

K-means clustering will be repeated on the MUC to locate the unstable link. Fig. 12 shows the flowchart of our clustering approach using the proposed joint space–time observation vector.

The following steps show how the clustering process is carried out.

1) Construct an $(n+2)$-dimensional joint observation vector that consists of n-consecutive time-based voltage amplitudes, $V_i = [V_{t-n+1,i}, V_{t-n+2,i}, \ldots\ldots, V_{t,i}]$ of the received PMUs' data and their corresponding 2-D locations, $D_i = [D_{x,i}, D_{y,i}]$.
2) Find similar pairs and dissimilar pairs by checking if $\|V_i - V_j\| < V_{\text{threshold}}$ and $\|D_i - D_j\| < D_{\text{threshold}}$.
3) Create a similarity matrix S and a dissimilarity matrix D based on the information provided by the similar pairs and dissimilar pairs.
4) Iteratively derive the rescale matrix A by employing the Newton–Raphson method.
5) Rescale the observation matrix ST in (28) to get a rescaled observation matrix: $Y = ST * A(1/2)$.
6) Carry out K-means clustering on the rescaled observation matrix Y.
7) Check the number of assigned observation vectors in every cluster.
   a) When $m_k \geq m_{\text{threshold}}$ in cluster C_k, calculate its standard deviation SD_k. If $SD_k > SD_{\text{threshold}}$, repeat K-means clustering on cluster C_k to locate the unstable links/regions. Otherwise, cluster C_k will be labeled as a stable cluster and have no more clustering.
   b) When $m_k < m_{\text{threshold}}$, use only the time-based observation vector V_i $(i = 1, 2, \ldots, m_k)$ that corresponds to $Y_i \in C_k$ for another round of clustering. Calculate cluster $\overline{C}_k$'s distance to the nonfaulted balanced vector V_{balance} and find the MUC. Repeat K-means clustering on the MUC to locate the unstable links/regions.

Before accessing the performance of the proposed classification algorithm, we first describe our hardware-in-loop testbed design, which is presented next.

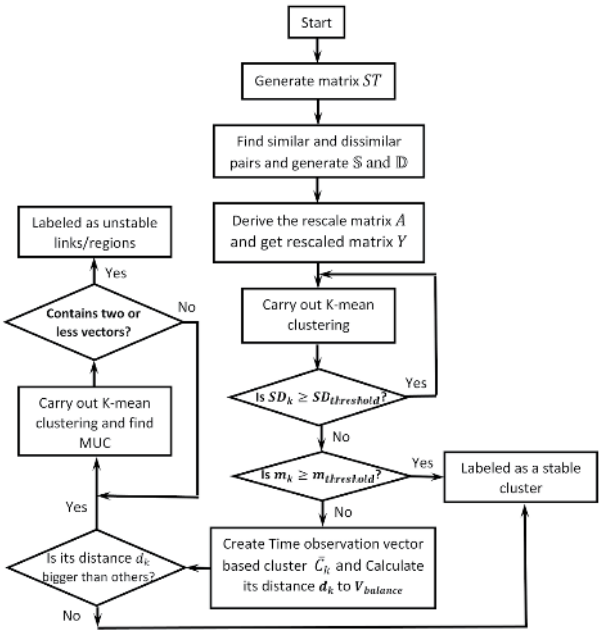

Fig. 12. ***Flowchart of the global distance metric learning based space–time clustering.***

V. HARDWARE-IN-THE-LOOP TESTBED DESIGN AND PERFORMANCE EVALUATION

So far, much research has concentrated on how to perform efficient simulation in terms of accuracy, runtime, etc. The main problem with simulation is that results cannot truly represent performance under real-world conditions. Even designing experiments to verify protocols or test new algorithms cannot be accurately conducted using simulation alone. This is mainly due to the complexity of synchrophasor operational environments, which require accurate modeling of both power grid and communication networking. With widening PMU applications and installations in massive numbers, future PMU characteristics will require better accuracy and higher frame rates, hence demanding an even higher communication bandwidths. Using only hardware to implement a testbed for integrated grid and communication network applications poses a significant challenge in terms of cost, effort, time, and more importantly, better flexibility for evaluation of new schemes and communication protocols under various test environments.

Our objective has been to design hardware-in-the-loop testbed that can support all the important functionality required for an integrated grid and communication networking testbed with the following features:

- capability to install an unlimited number of commercial PMU devices;
- use of VPMUs to test a large network;
- coexistence of both commercial PMU and VPMU for test and calibration;
- use of Emulab switches [86], [87] to support the network layer for real-time communications;
- use of GPS signaling for time synchronization for both commercial and VPMU;
- use of simulation tools for molding grid networks at the application layer;
- support of M2M wireless sensor networks.

A general block diagram of the hardware-in-the-loop testbed is shown in Fig. 13. In addition, Fig. 14 shows further details of the integrated grid communication network that includes options for using commercial PMUs and VPMUs. As can be observed from this figure, the testbed consists of

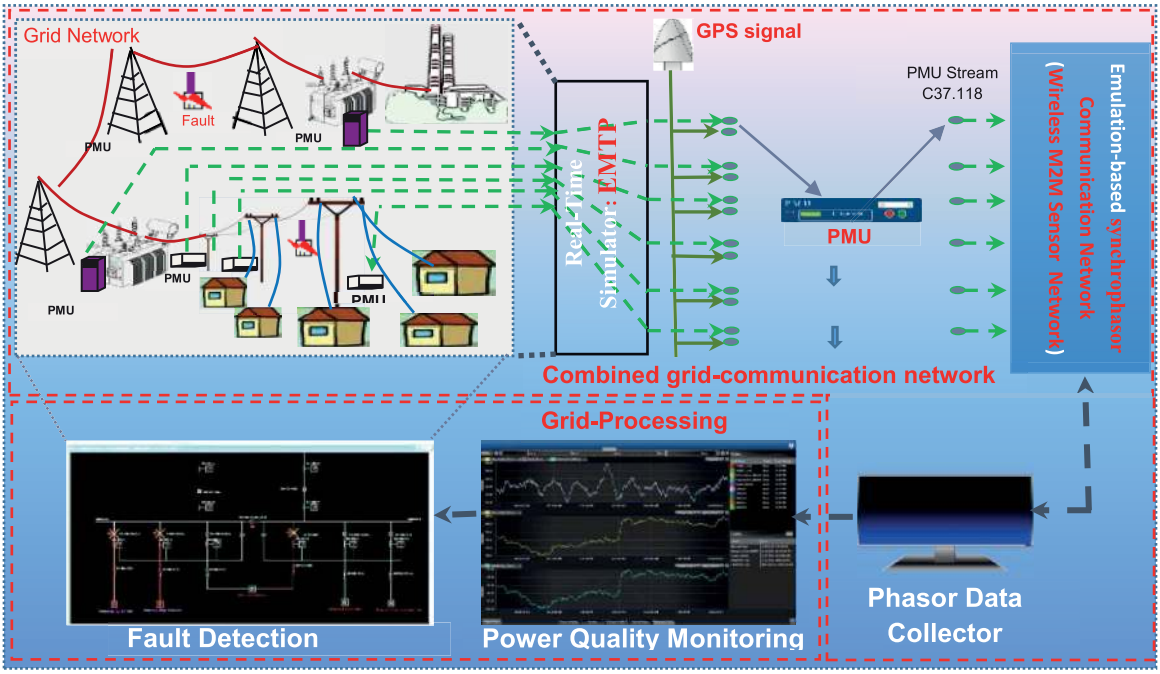

Fig. 13. ***Hardware-in-the-loop testbed, including the combined grid-communication network and grid processing, where the synchrophasor communication network, which is part of the combined grid-communication network, is configured to a wireless M2M sensor network.***

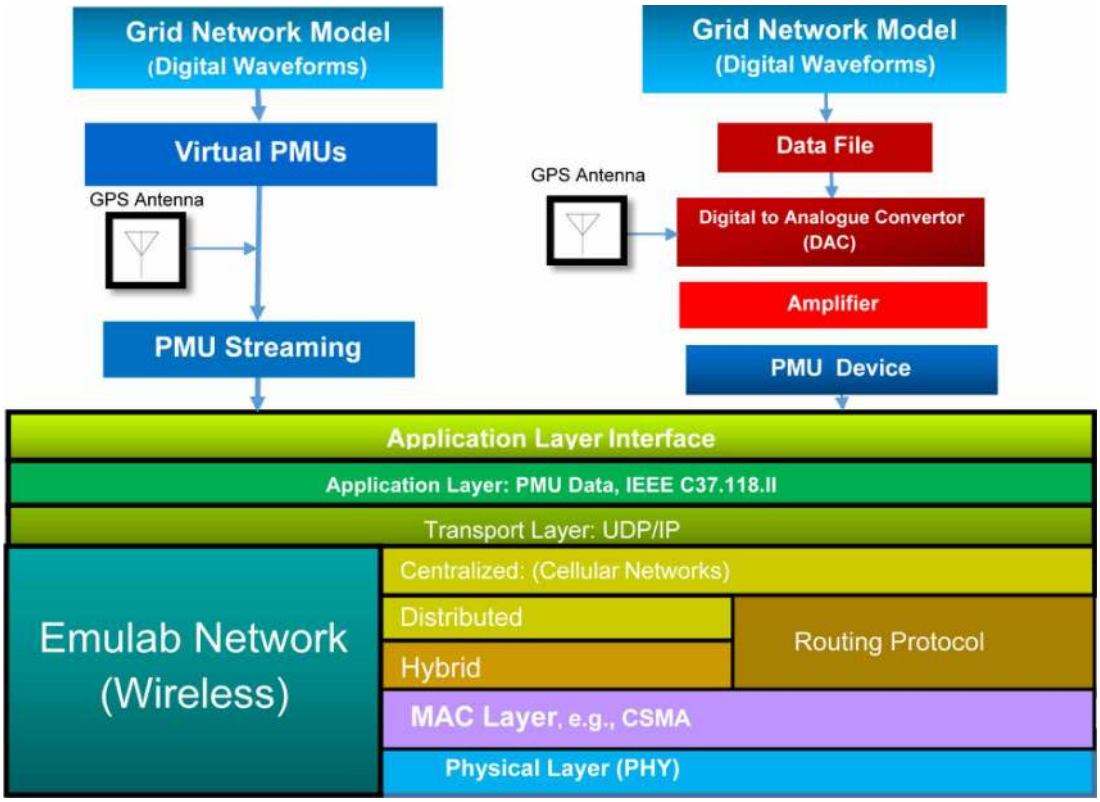

Fig. 14. ***An integrated grid communication network that can include commercial PMUs and VPMUs.***

a software-based grid network modeling using the Electro Magnetic Transients Program (EMTP) software[1] tool where PMU nodes can be placed at any desirable location in the grid network. EMTP [86]–[89] has been widely used as the time domain transient solution. It is able to provide almost all power system components, such as power plant, transformer, windfarm, different kinds of faults, overhead lines with line and ground wires and towers, as well as underground cables [90]. In this paper, EMTP is used to simulate the IEEE 39-bus transmission system and the 390-bus system where PMUs are placed on the buses of simulated power systems to collect and process samples of power signals. It should be noted that EMTP can only generate a sampled data of the current and voltage waveforms at each selected location. In contrast, an actual PMU only receives analog waveforms, which are then passed through an ADC to produce digitized output. As shown in Fig. 4, the ADC is an integral part of the PMU where the sampling clock is phase-locked with a 1-PPS GPS signal.

Therefore, to install a PMU device in the testbed, the sampled data generated by the EMTP should first be converted to analog waveforms before they can be fed to a commercial PMU. To achieve this, the data generated simultaneously at various locations in the EMTP grid network are first stored into separate files for a predefined testing period. For real-time operation, the synchrophasor data stored in these files should simultaneously release their data, which is coordinated with the GPS signaling. Subsequently, each file, which corresponds to a PMU at a specific location in the grid, has to pass through an external digital-to-analog converter (DAC) so that the generated analog waveforms can then be fed to each PMU devise in the testbed. However, as shown in Fig. 14, the DAC output may have to be further amplified in order to reach the input level specified by the PMU manufacturer. Under these conditions, each PMU will then provide measurement data, which include frequency and rate of change of frequency (ROCOF or DFREQ) in accordance with the IEEE C37.118 standard [49], [50]. It should be noted that PMU manufactures use their own propitiatory algorithms for frequency estimation as long as they are within performance metrics—TVE specified by the IEEE C37.118-1 standard [49]. Based on C37.118-2 [50], the PMU data are then encapsulated into a data frame for transmission to the PDC. IEEE C37.118 also defines PDC-to-PDC communication protocols where the aggregated data received from multiple PMUs can be forwarded to the utility PDC.

Although commercial PMUs can be installed in the testbed, their deployment in large quantities would not be cost effective. This is mainly due to the fact that using commercial equipment, such as PMUs as well as other supporting items such as DACs and amplifiers, is relatively expensive. Therefore, to evaluate the performance of a grid network for monitoring a larger network, we consider developing a VPMU. The ability to use commercial PMUs in the testbed would permit us to calibrate a VPMU's performance accordingly. Fig. 14 shows the deployment of both types of PMUs in the testbed. One major advantage of using VPMU is its programmability, which allows testing a grid network under extreme conditions. Bear in mind that high-voltage transmission systems have different operational characteristics than those of distribution systems. As mentioned before, the presence of noise and harmonics imposes many challenges to tracking the voltage and frequency variations. In addition, the distribution system may also suffer from excessive reactive power due to the presence of a nonlinear load. Indeed, these new requirements have been the main motivation for designing a VPMU where more robust frequency estimations (with the inclusion of PF in the measurement) can then be tested. The main advantage of a programmable VPMU lies in its ability to operate in real time. In other words, VPMU should be able to handle more complex frequency estimation algorithms, as well as high speed data streaming for real-time communications.

[1]Certain commercial equipment, instruments, or materials are identified in this paper to foster understanding. Such identification does not imply recommendation or endorsement by the National Institute of Standards and Technology, nor does it imply that the materials or equipment identified are necessarily the best available for the purpose.

A. Synchrophasor Communication Network Evaluation

In this section, we evaluate the performance of synchrophasor communication networks implementing IEEE 802.11ah. Scenarios with different RAW configurations are investigated and compared in order to find the best configuration for synchrophasor networks operating in IEEE 802.11ah mode.

Table 1 displays some of the important PHY and MAC layer parameters employed in our model. Communication among PMUs and a local PDC is accomplished through IEEE 802.11ah. The wireless link's bandwidth is set to operate at 2 Mb/s. The noise figure is 3.0 dB and the frequency is 900 MHz. The beacon interval and the RAW group duration are set to 0.1 s. The packet payload size is set to 64 B, which is the packet size of a C37.118 data frame sent by PMUs to PDCs. PMUs are randomly distributed in a circle around the PDC (AP) within a distance of 500 m. The retransmission limit is set at 1, based on the consideration that when a packet is lost it may not be necessary to retransmit it since the data packet with a next time stamp is expected to arrive via the next data frame [25]. A small buffer space is used to reduce latency. A set of sampling rates, namely 10, 20, 30, and 60 frames/s is used to evaluate the network performance in terms of throughput and packet loss. Throughput is the amount of data packets successfully received by an AP per second, and is measured in megabits per second. Packet loss rate is the percentage of packets lost with respect to packets sent.

In Figs. 15 and 16, the throughput and average end-to-end delay performance is evaluated for a synchrophasor network where 144 PMUs periodically generate and send data packets (synchrophasor measurements) to a local PDC (AP). Three RAW configurations (shown in Fig. 10)

Table 1 Default PHY and MAC Layer Parameters Used in Our Experiments

Parameter	Value	Parameter	Value
Frequency (Mhz)	900	MAC header type	legacy header
Channel Coding	Binary Convolutional Coding (BCC)	Beacon Interval (s)	0.1
Noise Figure (dB)	3	RAW group duration (s)	0.1
Propagation loss model	Outdoor, macro	Wi-Fi mode	MCS3, 2 Mhz
Error Rate Model	YansErrorRate [91]	Payload size (bytes)	64
CWmin	15	Cross slot boundary	enabled
CWmax	1023	Rate control algorithm	constant
AIFSN	3		

are investigated: configuration A with 144 RAW groups each containing a single slot, configuration B with 1 RAW group and each consists of 144 slots, and configuration C with 1 RAW group with a single slot. Figs. 15 and 16 show that configuration A and configuration B can produce better results, while configuration C indicates the worst performance. This is due to the fact that assigning PMUs into RAW groups reduces contention, hence lowering collision probability. More groups and slots result in a better performance, as long as the duration of each slot is large enough for one packet transmission.

These preliminary experimental results indicate that IEEE 802.11ah is capable of handling real-time PMU communications, as long as the frame rates and number of PMUs are carefully selected. We should emphasize that one of the main features of the IEEE 802.11ah standard is its operation in the sub-1-GHz spectrum. This improves the transmission range considerably as compared to other IEEE 802.11 WLANs, which are operating in 2.4- and 5-GHz bands. To a large extent, such an important feature can overcome the need for using multihop transmission, which renders itself susceptible to more delay and packet loss, as we previously experienced [25]. In addition, as described above, exploiting the new RAW channel access mechanism introduced in this standard has made a significant impact on the overall network performance especially in terms of overhead and latency, which would be crucial for a timely assessment of power quality.

B. Voltage Instability Assessment

Next, we assess the performance of the proposed synchrophasor data partitioning scheme using the IEEE 39-bus [92], [93] transmission and the 390-bus [86] systems shown in Figs. 17 and 18, respectively. While PMUs can be placed optimally [6-10], our main objective has been mainly to assess the performance of the proposed scheme under various test conditions. We used our real-time hardware-in-the-loop testbed-based synchrophasor network testbed [94], which utilizes the EMTP software package at the application layer that includes the IEEE 39-bus system and the 390-bus system. As described earlier, the testbed has the flexibility of installing a VPMU at any desirable location in both IEEE 39-bus and 390-bus systems. The VPMU has been carefully calibrated according to C37.118 [49], [50] for both measurements and real-time communications. The frame rate is set to 60 frames/s.

We first examine the performance of the joint space–time clustering technique for the IEEE 39-bus transmission system by imposing two sudden overload changes

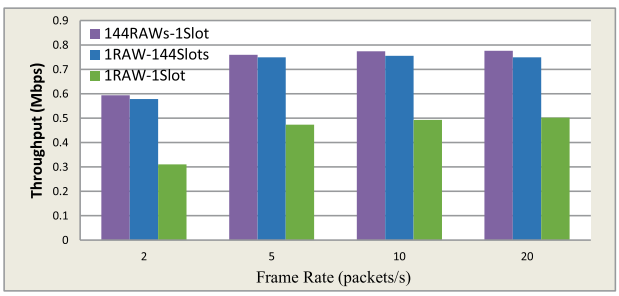

Fig. 15. *Throughput performance of the synchrophasor network operating in 802.11ah mode, where 144 PMUs periodically send synchrophsor data to a local PDC (AP).*

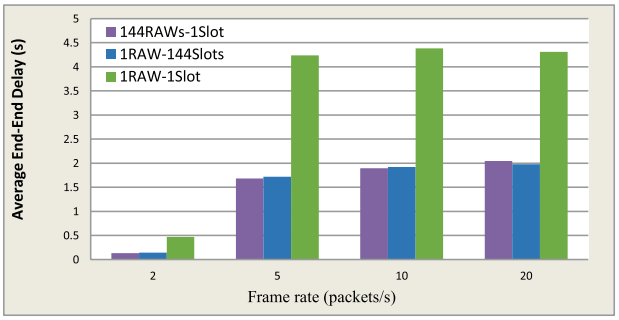

Fig. 16. *Average end-to-end delay performance of the synchrophasor network operating in 802.11ah mode, where 144 PMUs periodically send synchrophsor measurements to a local PDC (AP).*

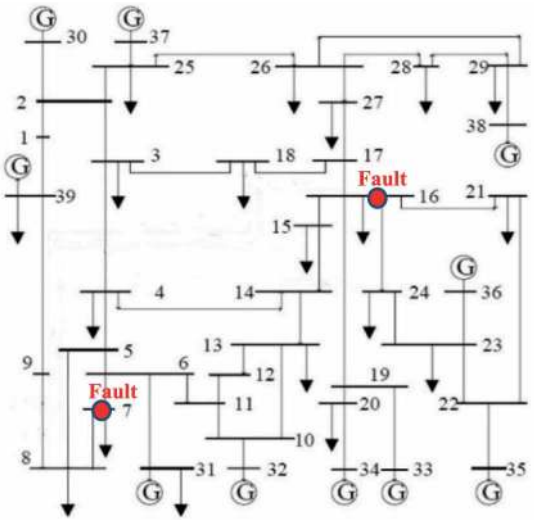

Fig. 17. ***The IEEE 39-bus transmission system.***

simultaneously on buses 7 and 16, as shown in Fig. 17. For our experiments, $m_{\text{threshold}} = 6$ and $SD_{\text{threshold}} = 0.5$ have been selected. Table 2 shows an example of a joint space–time observation vector. Based on similarity matrix S and dissimilarity matrix D, rescale matrix A can be derived based on the Newton–Raphson method

$$A = \begin{bmatrix} 1.00 & 0 & 0 & 0 & 0 & 0 & 0 \\ 0 & 0 & 0 & 0 & 0 & 0 & 0 \\ 0 & 0 & 9.90 & 0 & 0 & 0 & 0 \\ 0 & 0 & 0 & 14.0 & 0 & 0 & 0 \\ 0 & 0 & 0 & 0 & 0 & 0 & 0 \\ 0 & 0 & 0 & 0 & 0 & 0.38 & 0 \\ 0 & 0 & 0 & 0 & 0 & 0 & 1.27 \end{bmatrix}.$$

After deriving the rescaled matrix $= ST * A^{\frac{1}{2}}$, K-means clustering is performed to locate the unstable links/regions, as depicted in Fig. 19. In cluster-1, we have $m_k = 15 \geq m_{\text{threshold}}$ and $SD_k = 1.044 > SD_{\text{threshold}}$, which means that cluster-1 contains unstable links. Further K-means clustering is then carried out to locate them. The resulting cluster-1-2 has $m_k = 6 \geq m_{\text{threshold}}$ and $SD_k = 0.4558 < SD_{\text{threshold}}$, and is labeled as a stable cluster. On the other hand, since cluster-1-1 has $m_k = 9 \geq m_{\text{threshold}}$ and $SD_k = 0.8841 > SD_{\text{threshold}}$, K-means clustering will continue. Both cluster-1-1-1 and cluster-1-1-2 have smaller standard deviations than $SD_{\text{threshold}}$ and fewer vectors than $m_{\text{threshold}}$. The corresponding voltage clusters $\overline{C}_{1-1-1}$

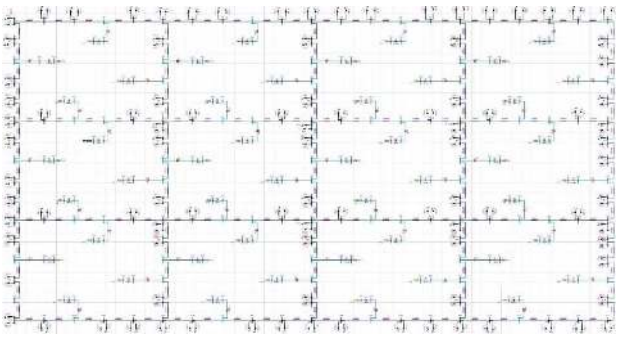

Fig. 18. ***The 390-bus system.***

Table 2 The Joint Space–Time Observation Vectors for the IEEE 39-Bus System

Bus	V_{-4}	V_{-3}	V_{-2}	V_{-1}	V_0	D_x	D_y
1	1	0.761050033	0.759186393	0.759831124	0.969819666	0.3	1.35
2	1	0.659235810	0.653302016	0.652764741	0.943289874	1.0	0.82
3	1	0.491675871	0.484006642	0.483624602	0.920272422	1.2	1.6
4	1	0.455104111	0.448318893	0.447709482	0.923390633	1.1	3.12
5	1	0.466929328	0.461460580	0.460752041	0.931318341	0.9	3.5
6	1	0.278539293	0.273464124	0.272755318	0.832637523	1.2	3.92
7	1	0.136292343	0.145771852	0.146172596	0.921900688	1.1	4.1
8	1	0.226858147	0.220160184	0.219446326	0.83184428	0.95	4.33
9	1	0.545170728	0.538685698	0.537957062	0.961887533	0.3	3.74
10	1	0.501304763	0.497179946	0.496538690	0.932433096	2.55	4.12
11	1	0.493134621	0.488788826	0.488134884	0.93261217	1.91	3.98
12	1	0.486021105	0.483392527	0.482759357	0.934924596	2.3	3.76
13	1	0.476062822	0.471847933	0.471224858	0.928613719	2.61	3.45
14	1	0.416353916	0.468665819	0.468062561	0.927832739	2.72	3.11
15	1	0.210647990	0.207339147	0.206968439	0.882956923	2.9	2.25
16	1	0.128442950	0.132180462	0.131734924	0.866305842	3.3	2.07
17	1	0.279945352	0.275384525	0.275281920	0.889133787	3.2	1.6
18	1	0.461069582	0.454184471	0.454053654	0.910370082	2.5	1.6
19	1	0.487755650	0.481564659	0.479467552	0.904822371	3.34	3.83
20	1	0.466904629	0.457590443	0.454067916	0.890655309	3.1	4.01
21	1	0.206795588	0.201730213	0.199572400	0.874695378	4.8	2.1
22	1	0.314184297	0.306470828	0.303925321	0.884096559	4.7	4.05
23	1	0.293754457	0.285614693	0.284052179	0.883614914	4.53	3.7
24	1	0.143015283	0.143165332	0.142320032	0.866907303	3.53	2.2
25	1	0.668680589	0.664837987	0.664567279	0.944600092	1.3	0.6
26	1	0.558276701	0.551514738	0.551587814	0.927747456	3.0	0.5
27	1	0.432654840	0.425119308	0.425138286	0.909813415	3.2	1.05
28	1	0.673327267	0.667138563	0.667595378	0.944311756	4.51	0.49
29	1	0.706947862	0.702046397	0.702730933	0.951454062	4.7	0.52
39	1	0.819255887	0.817580970	0.819491192	0.981569447	0.1	1.61

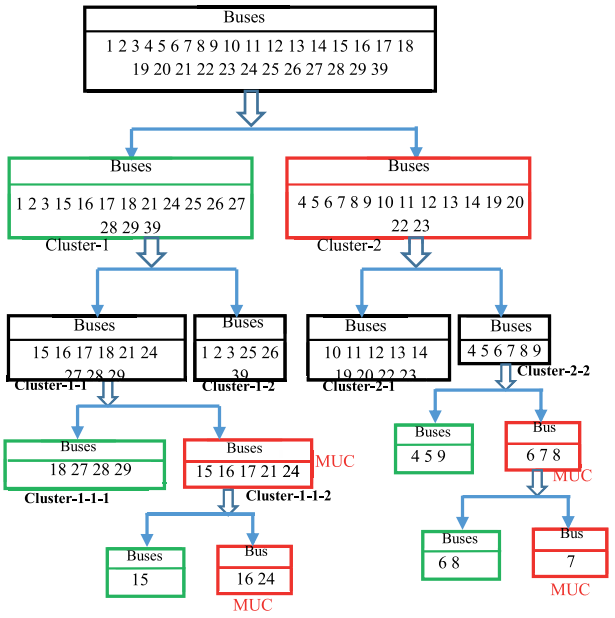

Fig. 19. ***The global distance metric learning-based space–time clustering for the IEEE 39-bus system.***

(including the voltage observation vectors of buses 18, 27, 28, and 29) and $\overline{C}_{1-1-2}$ (including voltage observation vectors of buses 15, 16, 17, 21, and 24) are generated and their distance to no-fault balanced vector V_{balance} is calculated. $\overline{C}_{1-1-2}$ has 1.4045 to V_{balance}, which is larger than that of $\overline{C}_{1-1-1}$ (0.7579). Therefore, $\overline{C}_{1-1-2}$ is treated as an MUC and undergoes another round of K-means clustering to identify the unstable links, which is between buses 16 and 24 (see Fig. 19). Cluster-2 also undergoes a similar procedure that locates bus 7 as an unstable bus.

The proposed clustering scheme is further evaluated using a 390-bus system. In this scenario, we impose the occurrences of three simultaneously fault incidents on buses 52, 103, and 129. In this experiment, 144 PUMs are deployed throughout the entire system. The corresponding rescale matrix A is derived as

$$A = \begin{bmatrix} 1.00 & 0 & 0 & 0 & 0 & 0 & 0 \\ 0 & 0 & 0 & 0 & 0 & 0 & 0 \\ 0 & 0 & 1.11 & 0 & 0 & 0 & 0 \\ 0 & 0 & 0 & 1.25 & 0 & 0 & 0 \\ 0 & 0 & 0 & 0 & 1.27 & 0 & 0 \\ 0 & 0 & 0 & 0 & 0 & 1.01 & 0 \\ 0 & 0 & 0 & 0 & 0 & 0 & 0.99 \end{bmatrix}.$$

Undergoing a similar procedure as in the 39-bus system, we can locate unstable buses 52, 103, and 129 as demonstrated in Fig. 20. However, we should point out that throughout these experiments, we never observed a convergence to a local minimum that can result in generating unstable partitions. In fact,

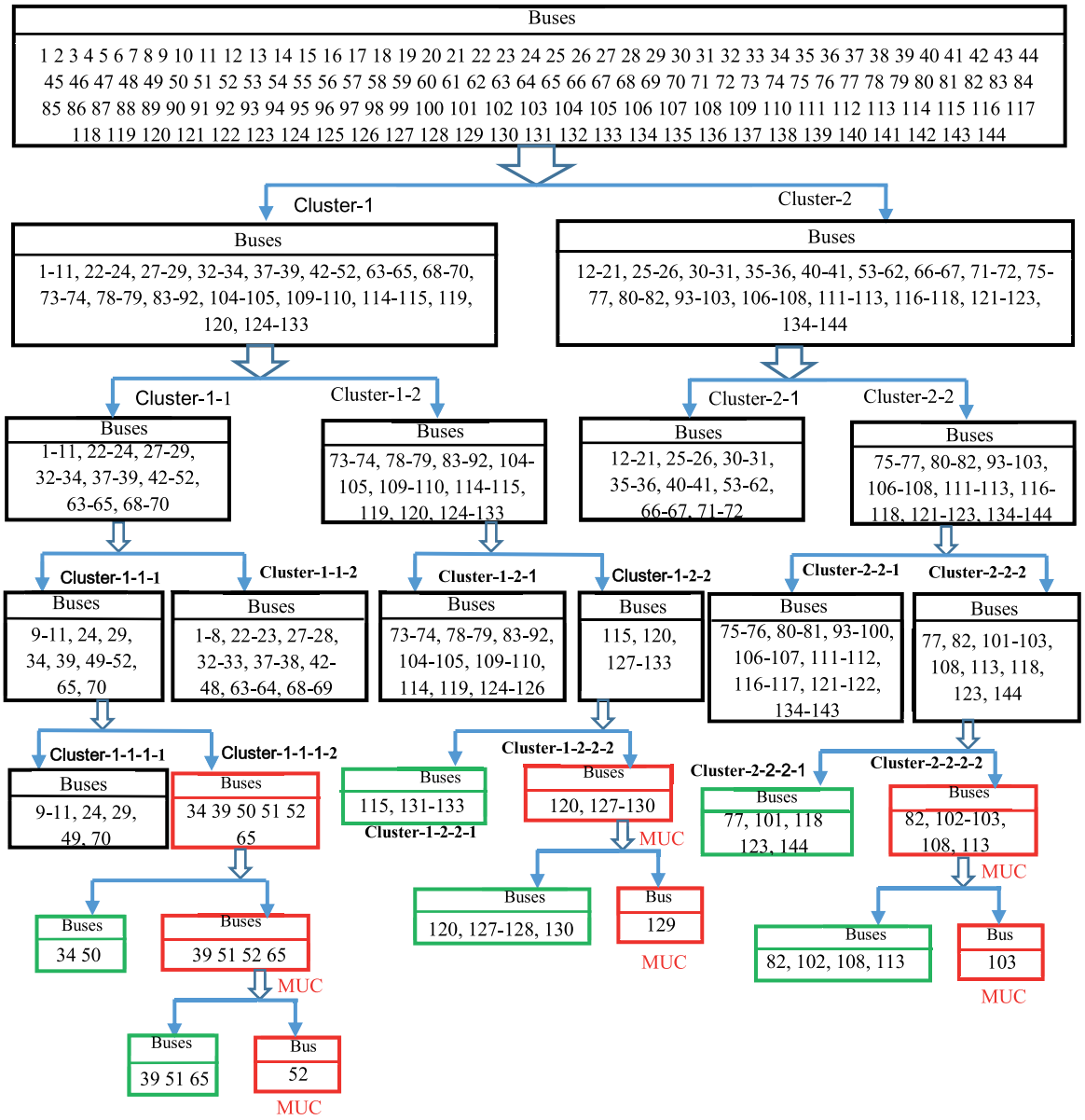

Fig. 20. ***The global distance metric learning-based space–time clustering for the 390-bus system with three simultaneous faults on buses 52, 103, and 129.***

the main reason behind using the 390-bus system was to generate more synchrophasor data sets. The proposed synchrophasor classifications method, which is based on the Newton–Raphson method, has also been compared with our earlier space–time approach [48]. In the latter, we mainly focused on selecting a suitable set of initial centroid values to perform a faster convergence, as well as reducing the possibility of locking into a local minimum. Nonetheless, for both methods the outcome in detecting the faulty regions turned out to be the same. However, based on the space–time concept, our main objective in this paper was to offer an alternative solution to the synchrophasor data partitioning for power quality monitoring and fault detection applications. It is worth mentioning that the proposed method, by creating a joint space–time observation vector, has the advantage of performing space–time clustering using a single observation input.

Finally, we should point out that future power quality monitoring for the distributed generation grid faces many challenges that will require a new paradigm for designing PMUs. For instance, the next-generation synchrophasor devices, called micro-PMUs (μPMU), should be able to estimate not only the fundamental frequency in the presence of noise, but also harmonics. In addition, as voltage stability is highly correlated to reactive power consumption, controlling it in real time is crucial to balancing electricity flow in a timely manner. Therefore, measuring TPF (described in Section II) as part of synchrophasor measurements can be instrumental to control reactive power and improve grid resilience.

VI. CONCLUSION

Grid protection is one of the key elements of critical infrastructure resilience. An important aspect of grid protection is outage management to prevent a cascading failure in the grid network. Today, with the ever increasing deployment of PMUs, the dynamic is shifting toward situational awareness through a wide area measurement system. A key aspect of situational awareness is to attain knowledge of the grid status. While PMUs are highly capable of providing synchronous measurement data, a major obstacle is determining how they can be effectively utilized to assess power quality, as well as detecting and locating various disturbances in the grid.

This paper focuses primarily on leveraging synchronized current/voltage amplitudes and phase angle measurements for grid protection. The motivation for such an application arises from the fact that with the support of communication networks, synchronized measurements from multiple sites in the grid network can greatly enhance the accuracy and timeliness of identifying the source of instabilities. The paper first provides a hardware-in-the-loop testbed implementation that is capable of performing an end-to-end assessment of the grid and communication networks in real time and under various test conditions. An important part of the investigation is the deployment of the emerging IEEE 802.11ah WLAN standard that can support a wide variety of sensory devices, including PMUs. This standard was found to be particularly suitable for synchrophasor networks due to its highly efficient access method. In addition, its very low energy consumption (adopted by a new power saving strategy) would allow sensor nodes to operate longer under blackout conditions.

Power quality monitoring and fault detection has also been another challenging issue covered here. We present a strategy for identifying regions that suffer from a rapid voltage fluctuation. This strategy, which is based on a space–time classification algorithm, uses a joint space–time observation vector to detect multiple sources of voltage instability.

REFERENCES

[1] V. Terzija *et al.*, "Wide-area monitoring, protection, and control of future electric power networks," *Proc. IEEE*, vol. 99, no. 1, pp. 80–93, Jan. 2011.

[2] B. Milosevic and M. Begovic, "Voltage-stability protection and control using a wide-area network of phasor measurements," *IEEE Trans. Power Syst.*, vol. 18, no. 1, pp. 121–127, Feb. 2003.

[3] M. Zima, M. Larsson, P. Korba, C. Rehtanz, and G. Andersson, "Design aspects for wide-area monitoring and control systems," *Proc. IEEE*, vol. 93, no. 5, pp. 980–996, May 2005.

[4] J. De La Ree, V. Centeno, J. S. Thorp, and A. G. Phadke, "Synchronized phasor measurement applications in power systems," *IEEE Trans. Smart Grid*, vol. 1, no. 1, pp. 20–27, Jun. 2010.

[5] A. G. Phadke, "The wide world of wide-area measurement," *IEEE Power Energy Mag.*, vol. 6, no. 5, pp. 52–65, Sep./Oct. 2008.

[6] V. Kekatos, G. B. Giannakis, and B. Wollenberg, "Optimal placement of phasor measurement units via convex relaxation," *IEEE Trans. Power Syst.*, vol. 27, no. 3, pp. 1521–1530, Aug. 2012.

[7] F. Aminifar, C. Lucas, A. Khodaei, and M. Fotuhi-Firuzabad, "Optimal placement of phasor measurement units using immunity genetic algorithm," *IEEE Trans. Power Del.*, vol. 24, no. 3, pp. 1014–1020, Jul. 2009.

[8] T. L. Baldwin, L. Mili, M. B. Boisen, Jr., and R. Adapa, "Power system observability with minimal phasor measurement placement," *IEEE Trans. Power Syst.*, vol. 8, no. 2, pp. 707–715, May 1993.

[9] W. Yuill, A. Edwards, S. Chowdhury, and S. P. Chowdhury, "Optimal PMU placement: A comprehensive literature review," in *Proc. IEEE Power Energy Soc. General Meeting*, San Diego, CA, USA, Jul. 2011, pp. 1–8.

[10] H. Nazaripouya and S. Mehraeen, "Optimal PMU placement for fault observability in distributed power system by using simultaneous voltage and current measurements," in *Proc. IEEE Power Energy Soc. General Meeting*, Vancouver, BC, USA, Nov. 2013, pp. 1–6.

[11] J. Chen and A. Abur, "Placement of PMUs to enable bad data detection in state estimation," *IEEE Trans. Power Syst.*, vol. 21, no. 4, pp. 1608–1615, Nov. 2006.

[12] S. M. Amin and B. F. Wollenberg, "Toward a smart grid: Power delivery for the 21st century," *IEEE Power Energy Mag.*, vol. 3, no. 5, pp. 34–41, Sep./Oct. 2005.

[13] Y.-F. Huang, S. Werner, J. Huang, N. Kashyap, and V. Gupta, "State estimation in electric power grids: Meeting new challenges presented by the requirements of the future grid," *IEEE Signal Process. Mag.*, vol. 29, no. 5, pp. 33–43, Sep. 2012.

[14] X. Bian, X. R. Li, H. Chen, D. Gan, and J. Qiu, "Joint estimation of state and parameter with synchrophasors—Part I: State tracking," *IEEE Trans. Power Syst.*, vol. 26, no. 3, pp. 1196–1208, Aug. 2011.

[15] E. Ghahremani and I. Kamwa, "Dynamic state estimation in power system by applying the extended Kalman filter with unknown inputs to phasor measurements," *IEEE Trans. Power Syst.*, vol. 26, no. 4, pp. 2556–2566, Nov. 2011.

[16] J. Giri, M. Parashar, J. Trehern, and V. Madani, "The situation room: Control center analytics for enhanced situational awareness," *IEEE Power Energy Mag.*, vol. 10, no. 5, pp. 24–39, Sep./Oct. 2012.

[17] J. D. Fernandez and A. E. Fernandez, "SCADA systems: Vulnerabilities and remediation," *J. Comput. Sci. Colleges Arch.*, vol. 20, no. 4, pp. 160–168, Apr. 2005.

[18] M. Chenine, E. Karam, and L. Nordstrom, "Modeling and simulation of wide area monitoring and control systems in IP-based networks," in *Proc. IEEE Power Energy Soc. General Meeting*, Calgary, AB, Canada, Jul. 2009, pp. 1–8.

[19] M. Wache and D. C. Murray, "Application of Synchrophasor Measurements for distribution networks," in *Proc. IEEE Power Energy Soc. General Meeting*, San Diego, CA, USA, Jul. 2011, pp. 1–4.

[20] A. von Meier, D. Culler, A. McEachern, and R. Arghandeh, "Micro-synchrophasors for distribution systems," in *Proc. IEEE Innov. Smart Grid Technol. Conf. (ISGT)*, Washington, DC, USA, Feb. 2014, pp. 1–5.

[21] H. Nazaripouya and S. Mehraeen, "Optimal PMU placement for fault observability in distributed power system by using simultaneous voltage and current measurements," in *Proc. IEEE Power Energy Soc. General Meeting*, Vancouver, BC, USA, Jul. 2013, pp. 1–6.

[22] J. Liu, J. Tang, F. Ponci, A. Monti, C. Muscas, and P. A. Pegoraro, "Trade-offs in PMU deployment for state estimation in active distribution grids," *IEEE Trans. Smart Grid*, vol. 3, no. 2, pp. 915–924, Jun. 2012.

[23] F. Katiraei and M. R. Iravani, "Power management strategies for a microgrid with multiple distributed generation units," *IEEE Trans. Power Syst.*, vol. 21, no. 4, pp. 1821–1831, Nov. 2006.

[24] M. Wache and D. C. Murray, "Application of Synchrophasor Measurements for distribution networks," in *Proc. IEEE Power Energy Soc. General Meeting*, San Diego, CA, USA, Jul. 2011, pp. 1–4.

[25] H. Gharavi and B. Hu, "Scalable synchrophasors communication network design and implementation for real-time distributed generation grid," *IEEE Trans. Smart Grid*, vol. 6, no. 5, pp. 2539–2550, Sep. 2015.

[26] H. Gharavi and B. Hu, "Hierarchical wireless network design for synchrophasor communication in distributed generation grid," in *Proc. IEEE Int. Conf. Commun. (ICC)*, London, U.K., Jun. 2015, pp. 808–814.

[27] A. Tiranuchit and R. J. Thomas, "A posturing strategy against voltage instabilities in electric power systems," *IEEE Trans. Power Syst.*, vol. 3, no. 1, pp. 87–93, Feb. 1988.

[28] M. Ettehadi, H. Ghasemi, and S. Vaez-Zadeh, "Voltage stability-based DG placement in distribution networks," *IEEE Trans. Power Del.*, vol. 28, no. 1, pp. 171–178, Jan. 2013.

[29] N. S. Rau and Y.-H. Wan, "Optimum location of resources in distributed planning," *IEEE Trans. Power Syst.*, vol. 9, no. 4, pp. 2014–2020, Nov. 1994.

[30] T. K. Panigrahi, S. Chowdhury, S. P. Chowdhury, N. Chakraborty, and Y. H. Song, "Control & reliability issue of efficient microgrid operation using hybrid distributed energy resources," in *Proc. IEEE PES Power Syst. Conf. Expo*, Atlanta, GA, USA, Nov. 2006, pp. 797–802.

[31] M. M. Albu, R. Neurohr, D. Apetrei, I. Silvas, and D. Federenciuc, "Monitoring voltage and frequency in smart distribution grids. A case study on data compression and accessibility," in *Proc. IEEE PES General Meeting*, Minneapolis, MN, USA, Jul. 2010, pp. 1–6.

[32] M. Prodanović, K. De Brabandere, J. Van den Keybus, T. Green, and J. Driesen, "Harmonic and reactive power compensation as ancillary services in inverter-based distributed generation," *IET Generat., Transmiss. Distrib.*, vol. 1, no. 3, pp. 432–438, May 2007.

[33] M. E. Baran and I. M. El-Markabi, "A multiagent-based dispatching scheme for distributed generators for voltage support on distribution feeders," *IEEE Trans. Power Syst.*, vol. 22, no. 1, pp. 52–59, Feb. 2007.

[34] L. B. Perera, G. Ledwich, and A. Ghosh, "Distribution feeder voltage support and power factor control by distributed multiple inverters," in *Proc. Electr. Power Energy Conf. (EPEC)*, Winnipeg, MB, Canada, Nov. 2011, pp. 116–121.

[35] T. Niknam, A. M. Ranjbar, and A. R. Shirani, "Impact of distributed generation on volt/Var control in distribution networks," in *Proc. IEEE Power Tech. Conf.*, Bologna, Italy, Jun. 2003, pp. 7–14.

[36] P. Hrisheekesha and J. Sharma, "Evolutionary algorithm based optimal control distribution system dispersed generation," *Int. J. Comput. Appl.*, vol. 14, pp. 31–37, Feb. 2010.

[37] Internet_of_Things. [Online]. Available: http://en.wikipedia.org/wiki/Internet_of_Things

[38] Z. M. Fadlullah, M. M. Fouda, N. Kato, A. Takeuchi, N. Iwasaki, and Y. Nozaki, "Toward intelligent machine-to-machine communications in smart grid," *IEEE Commun. Mag.*, vol. 49, no. 4, pp. 60–65, Apr. 2011.

[39] K. Chang, A. Soong, M. Tseng, and Z. Xiang, "Global wireless machine-to-machine standardization," *IEEE Internet Comput.*, vol. 15, no. 2, pp. 64–69, Mar./Apr. 2011.

[40] Y. K. Chen, "Challenges and opportunities of Internet of things," in *Proc. 17th Asia South Pacific Design Autom. Conf.*, Sydney, NSW, Australia, 2012, pp. 383–388.

[41] M. Hatton. *Machina Research: The Global M2M Market in 2013* http://www.telecomengine.com/sites/default/files/temp/CEBIT_M2M_WhitePaper_2012_01_11.pdf

[42] S. M. Babamir, "M2M Architecture: Can it realize ubiquitous computing in daily life?" *Trans. Internet Inf. Syst.*, vol. 6, no. 2, pp. 566–579, 2012.

[43] J. Gubbi, R. Buyya, S. Marusic, and M. Palaniswami, "Internet of Things (IoT): A vision, architectural elements, and future directions," *Future Generat. Comput. Syst.*, vol. 29, no. 7, pp. 1645–1660, 2013.

[44] L. Da Xu, W. He, and S. Li, "Internet of Things in industries: A survey," *IEEE Trans. Ind. Informat.*, vol. 10, no. 4, pp. 2233–2243, Nov. 2014.

[45] M. Zorzi, A. Gluhak, S. Lange, and A. Bassi, "From today's INTRAnet of things to a future INTERnet of things: A wireless- and mobility-related view," *IEEE Wireless Commun.*, vol. 17, no. 6, pp. 44–51, Dec. 2010.

[46] A. Laya, L. Alonso, and J. Alonso-Zarate, "Is the random access channel of LTE and LTE-A suitable for M2M communications? A survey of alternatives," *IEEE Commun. Surveys Tuts.*, vol. 16, no. 1, pp. 4–16, 1st Quart., 2014.

[47] M. Beale, "Future challenges in efficiently supporting M2M in the LTE standards," in *Proc. IEEE Wireless Commun. Netw. Conf. Workshops (WCNCW)*, Paris, France, Apr. 2012, pp. 186–190.

[48] H. Gharavi and B. Hu, "Space-time approach for disturbance detection and classification," *IEEE Trans. Smart Grid*, 2017, DOI: 10.1109/TSG.2017.2680742.

[49] *IEEE Standard for Synchrophasor Measurements for Power Systems, Revision of the IEEE Std. C37.118.2005, IEEE Standard C37.118.2011-1*, Dec. 2011.

[50] *IEEE Standard for Synchrophasor Data Transfer for Power Systems, Revision of the IEEE Std. C37.118.2005, IEEE Standard C37.118.2011-2*, Dec. 2011.

[51] *IEC Standard for Communication Network and Systems in Substations Part-9-2: Specific Communication Service Mapping (SCSM)-Sampled Values Over ISO/IEC 8802-3, IEEE Standard IEC 61850-9-2*, 2004.

[52] *IEEE Standard for a Precision Clock Synchronization Protocol for Networked Measurement and Control Systems, IEEE Standard 1588-2002*, 2002.

[53] M. M. Begovic, P. M. Djuric, S. Dunlap, and A. G. Phadke, "Frequency tracking in power networks in the presence of harmonics," *IEEE Trans. Power Del.*, vol. 8, no. 2, pp. 480–486, Apr. 1993.

[54] C. T. Nguyen and K. Srinivasan, "A new technique for rapid tracking of frequency deviations based on level crossings," *IEEE Trans. Power App. Syst.*, vol. 103, no. 8, pp. 2230–2236, Aug. 1984.

[55] M. S. Sachdev and M. A. Baribeau, "A new algorithm for digital impedance relays," *IEEE Trans. Power App. Syst.*, vol. PAS-98, no. 6, pp. 2232–2240, Nov. 1979.

[56] V. V. Terzija, M. B. Djuric, and B. D. Kovacevic, "Voltage phasor and local system frequency estimation using Newton type algorithm," *IEEE Trans. Power Del.*, vol. 9, no. 3, pp. 1368–1374, Jul. 1994.

[57] M. S. Sachdev, H. C. Wood, and N. G. Johnson, "Kalman filtering applied to power system measurements for relayingm," *IEEE Trans. Power App. Syst.*, vol. 104, no. 12, pp. 3565–3573, 1985.

[58] A. Routray, A. K. Pradhan, and K. P. Rao, "A novel Kalman filter for frequency estimation of distorted signals in power systems," *IEEE Trans. Instrum. Meas.*, vol. 51, no. 3, pp. 469–479, Jun. 2002.

[59] E. M. Siavashi, S. Afshania, M. T. Bina, M. K. Zadeh, and M. R. Baradar, "Frequency estimation of distorted signals in power systems using particle extended Kalman filter," in *Proc. 2nd Int. Conf. Power Electron. Intell. Transp. Syst.*, Dec. 2009, pp. 174–178.

[60] T. Lobos and J. Rezmer, "Real-time determination of power system frequency," *IEEE Trans. Instrum. Meas.*, vol. 46, no. 4, pp. 877–881, Aug. 1997.

[61] R. Vianello, M. O. Prates, C. A. Duque, A. S. Cequeira, P. M. da Silveira, and P. F. Ribeiro, "New phasor estimator in the presence of harmonics, dc offset, and interharmonics," in *Proc. 14th Int. Conf. Harmon. Quality Power.*, Sep. 2010, pp. 1–5.

[62] O. Chaari, M. Meunier, and F. Brouaye, "Wavelet: A new tool for the resonant grounded power distribution systems relaying," *IEEE Trans. Power Del.*, vol. 11, no. 3, pp. 1301–1308, Mar. 1996.

[63] J. F. Ren and M. Kezunovic, "Real-time power system frequency and phasors estimation using iterative wavelet transform," *IEEE Trans. Power Del.*, vol. 26, no. 3, pp. 1392–1402, Mar. 2011.

[64] H. Olkkonen and J. T. Olkkonen, "Log-time sampling of signals: Zeta transform," *Open J. Discrete Math.*, vol. 1, no. 2, pp. 62–65, 2011.

[65] I. Sadinezhad and V. G. Agelidis, "Extended staggered undersampling synchrophasor estimation technique for wide-area measurement systems," in *Proc. IEEE PES Innov. Smart Grid Technol.*, Perth, WA, Australia, Nov. 2011, pp. 1–7.

[66] C. Rusu and P. Kuosmanen, "Phase approximation by logarithmic sampling of gain," *IEEE Trans. Circuits Syst. II, Analog Digit. Signal Process.*, vol. 50, no. 2, pp. 93–101, Feb. 2003.

[67] S. Trittle and F. A. Hamprecht, "Near optimum sampling design and an efficient algorithm for single tone frequency estimation," *Digital Signal Process.*, Vol. 19, no. 4, pp. 628–639, 2009.

[68] J. Z. Yang and C. W. Liu, "A new family of measurement technique for tracking voltage phasor, local system frequency, harmonics and DC offset," *IEEE Power Eng. Soc. Summer Meeting*, vol. 3. Jul. 2000, pp. 1327–1332.

[69] B. Zeng, Z. S. Teng, Y. L. Cai, S. Y. Guo, and B. Y. Qing, "Harmonic phasor analysis based on improved FFT algorithm," *IEEE Trans. Smart Grid.*, vol. 2, no. 1, pp. 51–59, Mar. 2011.

[70] A. G. Phadke and B. Kasztenny, "Synchronized phasor and frequency measurement under transient conditions," *IEEE Trans. Power Del.*, vol. 24, no. 1, pp. 89–95, Jan. 2009.

[71] A. G. Phadke, J. S. Thorp, and M. G. A. Adamiak, "New measurement technique for tracking voltage phasors, local system frequency, and rate of change of frequency," *IEEE Trans. Power App. Syst.*, vol. PAS-102, no. 5, pp. 1025–1038, May 1983.

[72] G. Benmouyal, "An adaptive sampling-interval generator for digital relaying," *IEEE Trans. Power Del.*, vol. 4, no. 3, pp. 1602–1609, Jul. 1989.

[73] *IEEE Standard for Synchrophasor Measurements for Power Systems, Amendment 1: Modification of Selected Performance Requirements, IEEE Standard C37.118.1a-2014*, 2014.

[74] K. E. Martin, "Synchrophasor standards development-IEEE C37.118 & IEC 61850," in *Proc. 44th Hawaii Int. Conf. Syst. Sci.*, Jan. 2011, pp. 1–8.

[75] *Draft Standard for Information Technology-Telecommunications and Information Exchange Between Systems Local and Metropolitan Area Networks-Specific Requirements—Part 11: Wireless LAN Medium Access Control (MAC) and Physical Layer (PHY) Specifications—Amendment 2: Sub 1 GHz License ExemptOperation, IEEE Standard P802.11ah /D8.0.*

[76] E. Khorov, A. Lyakhov, A. Krotov, and A. Guschin, "A survey on IEEE 802.11ah: An enabling networking technology for smart cities," *Comput. Commun.*, vol. 58, pp. 53–69, Mar. 2014.

[77] L. Zheng, M. Ni, L. Cai, J. Pan, C. Ghosh, and K. Doppler, "Performance analysis of group-synchronized DCF for dense IEEE 802.11 networks," *IEEE Trans. Wireless Commun.*, vol. 13, no. 11, pp. 6180–6192, Nov. 2014.

[78] T. Adame, A. Bel, B. Bellalta, J. Barcelo, and M. Oliver, "IEEE 802.11AH: The WiFi approach for M2M communications," *IEEE Wireless Commun.*, vol. 21, no. 6, pp. 144–152, Dec. 2014.

[79] S. Aust, R. V. Prasad, and I. G. M. M. Niemegeers, "Outdoor long-range WLANs: A lesson for IEEE 802.11ah," *IEEE Commun. Surveys Tuts.*, vol. 17, no. 3, pp. 1761–1775, 3rd Quart., 2015.

[80] L. Tian, J. Famaey, and S. Latré, "Evaluation of the IEEE 802.11ah restricted access window mechanism for dense IoT networks," in *Proc. IEEE 17th Int. Symp. World Wireless, Mobile Multimedia Netw. (WoWMoM)*, Coimbra, Portugal, Jul. 2016, pp. 1–9.

[81] *IEEE Standard for Information Technology-Local and Metropolitan Area Networks- Specific Requirements-Part 11: Wireless LAN Medium Access Control (MAC)and Physical Layer (PHY) Specifications Amendment 4: Enhancements for Very High Throughput for Operation in Bands Below 6 GHz. IEEE Standard for Information Technology- Telecommunications and Information Exchange, IEEE Standard 802.11ac-2013*, p. 425, 2013.

[82] NarrowBand IoT (NB-IoT). 3GPP. (2015). *TSG RAN Meeting #69*, [Online]. Available: www.3gpp.org/FTP/tsg ran/TSG RAN/TSGR 69/Docs/RP-151621.zip

[83] H. Gharavi and B. Hu, "Wireless infrastructure M2M network for distributed power grid monitoring," *IEEE Netw. Mag.*, to be published.

[84] T. Adame, A. Bel, B. Bellalta, J. Barcelo, and M. Oliver, "IEEE 802.11AH: The WiFi approach for M2M communications," *IEEE Wireless Commun.*, vol. 21, no. 6, pp. 144–152, Dec. 2014.

[85] E. Xing, A. Ng, M. Jordan, and S. Russell, "Distance metric learning, with application to clustering with side-information," in *Proc. Conf. Adv. Neural Inf. Process. Syst. (NIPS)*, 2003.

[86] Emulab—Network Emulation Testbed Home. [Online]. Available: www.emulab.net

[87] B. White *et al.*, "An integrated experimental environment for distributed systems and networks," in *Proc. 5th Symp. Oper. Syst. Design Implement.*, Boston, MA, USA, Dec. 2002, pp. 255–270.

[88] H. W. Dommel, "Digital computer solution of electromagnetic transients in single-and multiphase networks," *IEEE Trans. Power App. Syst.*, vol. PAS-88, no. 4, pp. 388–399, Apr. 1969.

[89] H. W. Dommel, "EMTP theory book, Bonneville power administration," Conversion Into Electronic Format by Canadian/American EMTP Users Group, 1995.

[90] K. Fekete, S. Nikolovski, G. Knezević, M. Stojkov, and Z. Kovač, "Simulation of lightning transients on 110 kV overhead-cable transmission line using ATP-EMTP," in *Proc. Melecon 15th IEEE Medit. Electrotech. Conf.*, Valletta, Malta, Jul. 2010, pp. 856–861.

[91] M. Lacage and T. R. Henderson, "Yet another network simulator," in *Proc. Workshop NS-2, IP Netw. Simulator*, Pisa, Italy, 2006, p. 12.

[92] T. Athay, R. Podmore, and S. Virmani, "A practical method for the direct analysis of transient stability," *IEEE Trans. Power App. Syst.*, vol. PAS-98, no. 2, pp. 573–584, Mar./Apr. 1979.

[93] A. Pai, *Energy Function Analysis for Power System Stability*. New York, NY, USA: Springer-Verlag, 1989.

[94] Combined Grid Communication Testbed Implementation for Real-Time Measurement, Calibration, and Communication. [Online]. Available: https://www.nist.gov/programs-projects/combined-grid-communication-testbed-implementation-real-time-measurement

ABOUT THE AUTHORS

Hamid Gharavi (Fellow, IEEE) received the Ph.D. degree from Loughborough University, Loughborough, U.K. in 1980.

He joined the Visual Communication Research Department at AT&T Bell Laboratories, Holmdel, NJ, USA, in 1982. He was then transferred to Bell Communications Research (Bellcore), where he became a Distinguished Member of Research Staff. In 1993, he joined Loughborough University as a Professor and Chair of Communication Engineering. Since September 1998, he has been with the National Institute of Standards and Technology (NIST), U.S. Department of Commerce, Gaithersburg, MD, USA. He was a core member of Study Group XV (Specialist Group on Coding for Visual Telephony) of the International Communications Standardization Body CCITT (ITU-T). His research interests include smart grid, wireless multimedia, mobile communications and wireless systems, mobile *ad hoc* networks, and visual communications. He holds eight U.S. patents and has over 130 publications related to these topics.

Dr. Gharavi received the Charles Babbage Premium Award from the Institute of Electronics and Radio Engineering in 1986, and the IEEE CAS Society Darlington Best Paper Award in 1989. He served as a Distinguished Lecturer of the IEEE Communication Society. In 1992 he was elected a Fellow of IEEE for his contributions to low-bit-rate video coding and research in subband coding for video applications. He has been a Guest Editor for a number of special issues, including "Smart Grid: The Electric Energy System of the Future," Proceedings of the IEEE, June, 2011; and the "Special Issue on Sensor Networks & Applications," Proceedings of the IEEE, August 2003. He was a TPC Co-Chair for IEEE SmartGridComm in 2010 and 2012. He served as a member of the Editorial Board of Proceedings of the IEEE from January 2003 to December 2008. From January 2010 to December 2013 he served as the Editor-in-Chief of IEEE Transactions on CAS for Video Technology. He is currently serving as the Editor-in-Chief of IEEE Wireless Communications.

Bin Hu (Senior Member, IEEE) received the Ph.D. degree from the School of Electronics and Computer Science, University of Southampton, Southampton, U.K., in 2006.

Since September 2006, he has been with the National Institute of Standards and Technology, U.S. Department of Commerce, Gaithersburg, MD, USA, where he is currently a Research Scientist at the Advanced Network Technologies Division. His research interests include smart grid, video/image transmission, mobile communications, and mobile *ad hoc* networks.